REVIEWS OF TOPICAL PROBLEMS

Defect and track formation in solids irradiated by superhigh-energy ions

F F Komarov

Contents

Abstract. The state-of-the-art of research into processes and mechanisms of defect and track formation in materials irradiated by fast ions is reviewed. It is shown that the nature and morphology of tracks depend on the type and structure of the material and on the amount of energy density transferred to its electron subsystem. It is also shown that the relaxation of high electronic excitations dominates the track formation process. Discontinuous track formation mechanisms and those underlying the migration of atoms and the channeling of ions in tracks are discussed.

1. Introduction

For fast ions with kinetic energies $E \geqslant 1$ MeV a.m.u.$^{-1}$, the intensity with which energy is imparted to the electron subsystems, $(\mathrm{d}E/\mathrm{d}x)_{\mathrm{e}}$, is $10^3 – 10^4$ times higher than that of the of energy imparted to the nuclear subsystem of the solid. For instance, $(\mathrm{d}E/\mathrm{d}x)_{\mathrm{e}}$ amounts to $20 – 30$ keV nm^{-1} for heavy ions with a mass of about 100 a.m.u. and an energy $E \approx 1$ MeV a.m.u.$^{-1}$. The high rate of energy transfer to the electron subsystem enhances the role of electronic excitations in generating structural defects, causes intense inelastic sputtering of materials, and initiates a number of specific effects, such as track formation, local melting, amorphization, creation of extraordinary phases (high-pressure phases, fullerenes, and nanotubes), the generation of shock waves and destruction of materials. The most important and interesting result concerning the penetration of high-energy ions through solids is the formation of specific spatially distributed macrodefects, or tracks. Such defects are commonly known as latent tracks if they can be identified by chemical etching of the irradiated material. With some materials, most often with insulators, this technique is used to create various filters and microdiaphragms.

2. Effect of intense electronic excitations on transformation of the defect system in metals

Recently, there have been many investigations into the effect of a high density of electronic excitations on the generation of structural defects in metals or the transformation of defects created as a result of elastic collisions between the impinging ions and the target atoms. Some researchers (see Refs [1 – 17]) have found that high-density electronic excitations lead to defect formation in certain crystalline metals. For instance, Henry et al. [18] studied titanium irradiated by Pb ions with $E = 1 – 5$ GeV by using a transmission electron microscope (TEM). The inquiries demonstrated that dense agglomerates of defect clusters form along the direction of the ion beam. The magnitude of the defect-formation cross section σ, obtained from measurements of the electrical resistance at cryogenic

F F Komarov Belorussian State University
ul. Kurchatova 7, 220064 Minsk, Belarus'
Tel./Fax (+ 375-17) 277 48 33
E-mail: komarovf@bsu.by

temperatures, was found to be much larger than the theoretical prediction σ_{calc} obtained with allowance for only elastic displacements of the matrix atoms. The defect-formation efficiency ξ is defined as follows: $\xi = \sigma/\sigma_{calc}$. For instance, for Ti irradiated by 4.484-GeV ions of Pb, the value of ξ is as high as 21.5 [19, 20], while for the $Fe_{60}Co_{40}$ alloy irradiated by 445-MeV ions of Ag, the result is $\xi = 22.8$ [8].

The differences in defect formation in metals irradiated by heavy ions may be substantial [8, 10, 16, 18 – 21]:

(1) in some metals, such as Cu, W, Ag, and the ordered or disordered Cu_3Au alloy, only elastic collisions contribute to defect formation;

(2) in such materials as Ni, Pb, Pt, Nb, Ni_3Fe, austenites, and pure iron, there is partial annealing of the defects produced in elastic collisions. For iron, such a behavior is characteristic only in the $2.5 – 50$-keV nm^{-1} range of electronic stopping powers for ions;

(3) the high level of electronic excitations may be the cause of additional damage to such metals and alloys as Ga, Ti, Be, Sc, V, Cr, Mn, Re, Zr, Co, $Fe_{60}Co_{40}$, and Fe [when $(dE/dx)_e > 50$ keV nm^{-1}], as well as the semimetal Bi. For the $Fe_{60}Co_{40}$ alloy, the threshold stopping power at which the inelastic stopping of ions contributes to defect formation amounts to roughly 5 keV nm^{-1}.

The grading of materials by their sensitivity to electronic excitation is based on the maximum value of $(dE/dx)_e$ inherent in the beam of uranium ions with $E = 5$ MeV a.m.u.$^{-1}$ and may change if one adopts higher values of $(dE/dx)_e$, achieved through irradiation by cluster beams [12, 22] or by ions of radioactive elements with values of the atomic number Z higher than that of uranium. Such irradiation reduces the number of materials that were assumed insensitive to electron irradiation.

The data on defect formation in metals obtained in various experiments are listed in Table 1.

It is only natural to assume that in regions where the density of electronic excitations is high there are two processes that run simultaneously: defect production, and defect annealing. For instance, Dunlop et al. [23] and Dammak et al. [24] studied the transformation and annealing of defects produced during ion irradiation as a result of elastic processes. Iron specimens 11-μm thick were first irradiated by iron ions of different energies (polyenergetic implantation in the $10 – 170$-MeV range) at $T = 5$ K to create a homogeneous distribution of displacement cascades over the thickness and volume of the specimen. In the course of such treatment, both the electrical resistance of the specimens and their length increased.

The cascade regions that had not collapsed into dislocations were then bombarded by 500-MeV iron ions at $T = 5$ K. The decrease in resistance and length of foil specimens in the course of the second irradiation was interpreted as the collapse of the already produced defects into dislocation loops. The instability of the defect-containing regions is due to the transfer of some of the inelastic ion energy losses from the electron system to the lattice atoms, which changes the defect configurations. Thus, in metals, too, there are effects similar to track formation in insulators.

Table 1. Defect-formation efficiency for metals irradiated by high-energy ions at $T = 77$ K. The electronic stopping power $(dE/dx)_e$ is expressed in kiloelectron-volts per unit interatomic distance, and E_d is the threshold energy of displaced-atom formation.

Target	Ion	Ion energy, GeV	$(dE/dx)_e$, keV per u.i.d.	Thickness, μm	E_d, eV	$\sigma_{calc} \times 10^{-18}$, cm^2	ξ
Ag	O	0.165	0.399	11.75	39	0.705	0.63
	Pb	4.676	13.4	12		24.8	0.92
	Pb	3.521	14.62	11.2		29.4	0.82
W	O	0.119	0.736	10.7	50	1.09	0.52
	Pb	3.697	21.78	10.5		35	0.78
Pt	Pb	2.802	24.59	6.6	44	51	0.26
Pd	O	0.1145	0.474	8.3	41	0.72	0.73
	Pb	4.462	14.81	7.7		23.9	0.44
Ni	O	0.149	0.378	9.6	33	0.55	0.78
	Pb	4.056	12.24	10		19.2	0.64
	Pb	2.117	14.35	9.8		33	0.44
Co	O	0.177	0.325	5.54	36	0.4	0.57
	O	0.110	0.451	5.8		0.63	0.42
	Pb	4.847	11.14	5.65		14.1	4
Zr	O	0.177	0.274	8.2	28	0.77	0.81
	O	0.156	0.303	8.2		0.84	0.84
	Pb	4.087	10.11	8		30.5	2
Ti	O	0.166	0.189	13.5	17	0.71	0.84
	O	0.142	0.242	13.6		0.83	0.95
	Pb	4.484	7.18	13.8		27.5	21.5
$Fe_{60}Co_{40}$	N	0.04	2.4*	0.07	24	—	0.87
	N	0.186	0.93*	0.07		—	0.40
	Ag	0.445	33.9*	0.07		—	22.8

*Unit of measurement: keV nm^{-1}.

3. Track formation in metals and alloys and in compounds with metallic conduction

Another confirmation of the particular spatial localization of disturbances is the amorphization of metal alloys in the individual track region near the ion paths. Barbu et al. [16, 25] studied irradiated $NiZr_2$ alloys and were able to directly measure the average track diameter (≈ 4 nm), which corroborates the estimates of Dammak et al. [24]. The initially extended drop-like shape of the tracks gradually transforms into a continuous cylindrical shape as $(dE/dx)_e$ increases.

As in the case of insulators, latent tracks can be exposed in materials with metallic conduction by applying chemical etching followed by the capture of the image of the pattern by scanning electron microscopy (SEM) methods. For instance, Trautmann et al. [26] exposed, after applying selective etching in a solution of HCl or $FeCl_3$, the latent tracks in the amorphous metal alloy $Fe_{81}B_{13.5}Si_{3.5}C_2$ bombarded by ions of U, Bi, and Au with energies corresponding to values of $(dE/dx)_e$ ranging from 55 to 63 keV nm^{-1} (Fig. 1).

All tracks were etched at the same rate and had the same pore size. The annealing of the irradiated specimens had no effect on the etching rate. The etching rate in the disturbed areas was twice as high as in the nonirradiated part of the specimen. This suggests that the densities of the material in the track and in the nonirradiated areas are different. Latent tracks were not exposed by chemical etching when the target was bombarded by ions with $(dE/dx)_e = 24$ keV nm^{-1}, which points to the threshold nature of the chemical etching process.

Dunlop and Lesueur [27] observed amorphization in some conducting alloys (Ni-Zn, Ni-Ti), when the specimens were irradiated by ions with energies no lower than 1 GeV. Note that these metal targets become amorphous under low-energy ion irradiation ($E \leqslant 1$ MeV) either. However, complete amorphization is achieved under irradiation by heavy ions with energies $E \geqslant 1$ GeV and fluences corresponding to the calculated number of displacements per atom caused by elastic collisions; these fluences are at least a hundred times smaller than those required by low-energy ion implantation. Apparently, in such materials the stage of relaxation of

Figure 1. SEM micrograph of the surface of a $Fe_{81}B_{13.5}Si_{3.5}C_2$ specimen [26] which has a porous structure after ionic bombardment and etching. The irradiated (upper right and lower left) and nonirradiated (central) parts of the region are clearly distinguished (the length of the light dashes at the top is 10 μm).

electronic excitations is followed by a thermalization stage in the atomic subsystem of the track areas, with the latter stage similar to processes in the cascade regions in low-energy ion implantation.

Electronic excitations in metals lead to the formation of disturbances only when the energy density imparted to the electron subsystem is very high. For instance, discontinuous tracks are formed in $NiZr_2$, when the rate of energy transfer to electronic excitations exceeds 40 keV nm^{-1} [25], while the typical threshold values of $(dE/dx)_e$ for track formation in insulators are approximately 10 times lower. To examine in full the problem of defect formation in metals owing to electronic excitations, we must first classify the main processes: the relaxation of intense electronic excitations with a fraction of the energy transferred to the atomic subsystem, and the subsequent thermalization of the excited atoms with the excess of energy transferred to the surrounding matrix.

The first process is strongly determined by the type of material (metal, semiconductor, or insulator), the electron concentration in the conduction band (at the Fermi level), and the electron mobility. The transport of energy from the electron subsystem to the atomic one also depends on the type of material, the material's structural features (bulky material, thin film, size of grains in polycrystals, concentration and type of impurities, etc.). The thermalization process and the structural features of the region after 'cooling' is completed depend (just as they do in low-energy ion implantation) on the type of material, the type of crystal lattice, the ratio of the volumes of the material in the liquid and solid phases, and the presence of allotropic forms. The processes of energy transfer from electrons to lattice and the dissipation of the local stored lattice energy are usually estimated by an approach that allows for electron–electron and electron–phonon interactions [28–31].

Such an approach is not without its faults, since at a high level of electronic excitation (e.g., on stripping all electrons in a local area in the crystal near the ion path) or during formation of a dense cascade of atomic displacements in low-energy ion implantation, the existence of phonons can be assumed only with great reservation. In the latter case, the molecular dynamics method reveals a state of the cascade region (a thermal spike) resembling a liquid-like structure with a radial distribution function (and a static structural factor) similar to that of liquids [32]. Without postulating the existence of phonons and electron–phonon coupling at thermal spikes, Koponen [33] assumed that the cooling of such peaks is due to the interaction of the collective modes of ion motion in the cascade with the valence electrons of the metal. The collective modes of fluctuations of the ionic (atomic) density with short characteristic times (fractions of a picosecond) provide the mechanism for energy exchange with electrons, which is similar to electron–phonon interaction.

We believe that in both cases the first approach should be used to estimate the role of the type of material and the concentration and mobility of free electrons. The relaxation of the intense electronic excitations caused by the bombardment of the material with high-energy ions is the main factor determining the nature of the track region. In many pure coarse-grained metals (the grain size is much larger than the electron mean free path), the relaxation of the electronic excitations in the track region is determined by the electron heat conductivity. The energy transfer from hot electrons to
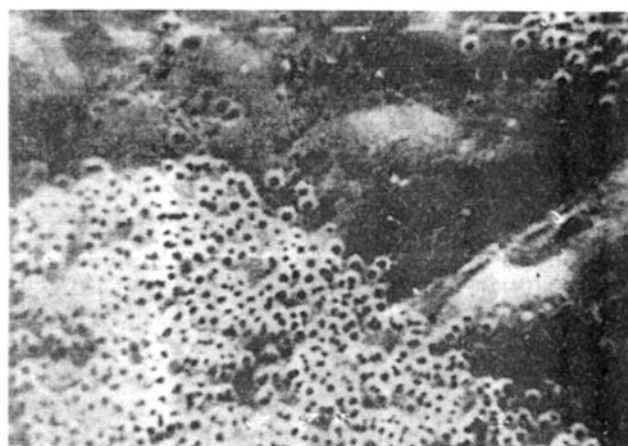
cold electrons increases the radius of the excitation region and drives the electron temperature inside this region down. The free path λ corresponding to this process at high temperatures ($T_e > \hbar\omega_p$, with $\hbar$ the Planck constant, T_e the electron temperature, and ω_p the plasma frequency) is determined by plasmon excitation ($\lambda = \lambda_p$), while as the temperature lowers the free path becomes related only to Coulomb collisions ($\lambda \approx \lambda_0$). Hence, the electron free path at an arbitrary temperature is given by the formula

$$\lambda = \frac{\lambda_0 \lambda_p}{\lambda_0 + \lambda_p} \,, \qquad (3.1)$$

while the electron thermal diffusivity in the metal is defined as

$$\chi = \frac{\langle v\lambda \rangle}{3} \,, \qquad (3.2)$$

where v is the electron velocity. The dependence of the thermal diffusivity of metals on the electron temperature, $\chi(T)$, is represented by a curve with a dip at $T_e > \varepsilon_F$ (ε_F is the Fermi electron energy), with the minimum thermal diffusivity χ_{min} being roughly 1 cm^2 s^{-1}, which is smaller by a factor of 100 than for metals under ordinary conditions.

Thus, the characteristic time it takes the electrons in the excited region of metals to cool off because of electron heat conductivity can be estimated as follows:

$$\tau_1 = \frac{R_{tr}^2}{4\chi_{min}} \approx 10^{-15} \text{ s} \,. \qquad (3.3)$$

Here $R_{tr} \approx 1$ nm is the radius of the cylindrical excited region. The electron–phonon relaxation time is roughly 10^{-12}–10^{-13} s [29, 31, 34]. The electron cooling time in such metals is much shorter than the electron–phonon relaxation time.

Lifshits et al. [28] described the process of formation and development of an energy track in metals in terms of the two-temperature model: they introduce the lattice temperature T_i and the electron temperature T_e, and then solve a system of two nonlinear heat conduction equations, which in cylindrical coordinates assumes the form

$$C_e(T_e) \frac{\partial T_c}{\partial t} = \frac{1}{r} \frac{\partial}{\partial r} \left(r K_e(T_e) \frac{\partial T_e}{\partial r} \right) - g(T_e - T_i) + A(r, t),$$

$$C_i(T_i) \frac{\partial T_i}{\partial t} = \frac{1}{r} \frac{\partial}{\partial r} \left(r K_i(T_i) \frac{\partial T_i}{\partial r} \right) + g(T_e - T_i), \qquad (3.4)$$

where C_k and K_k are the specific heat capacity and the heat conductivity, respectively; the subscript k corresponds to 'e' for the electron subsystem, and to 'i' for the ion (lattice) subsystem; g is the electron–phonon coupling constant, $A(r, t)$ is the density of the energy imparted by an impinging ion to the electron subsystem of the solid; r is the radial coordinate, and t is the time variable. Equations (4.1) are solved numerically, since their coefficients are temperature-dependent. Numerical calculations also make it possible to take into account the solid–liquid phase transition. The methods used in the numerical solution of this system of equations are discussed in Refs [31, 35, 36].

The main physical parameters and coefficients for the system of equations (3.4) must be examined in terms of the thermal spike model of track formation in metals. For pure metals, the lattice heat conductivity $K_a(T_a)$, the heat capacity $C_a(T_a)$, and the latent heats of melting and vaporization are known from the measurements done by Wang et al. [37] (for crystal atoms the subscript 'i' is replaced with 'a'). The parameters in the equations that are responsible for energy diffusion in the electron subsystem are defined in an approximation in which it is assumed that the electrons are similar to the 'quasi-free' electrons in a noble metal. The electron–phonon coupling constant is described with allowance for the physical properties of the irradiated material [10, 14].

In accordance with the theory of delta-electron formation accompanying the passage of swift electrons [38], we can write for the energy density:

$$A(r, t) = bS_e \exp\left(\frac{-(t - t_0)^2}{2t_0^2}\right) F(r) \,. \qquad (3.5)$$

Here, t_0 is the mean time of flight of the delta electrons, $t_0 \approx 1$–5×10^{-15} s (the choice of t_0 has only a small effect on the radius of the melt area [37]), $S_e = 1/N \, (dE/dx)_e$, where N is the number of atoms per unit volume of the stopping medium, and b is a normalization constant. The half-width of the Gaussian distribution is assumed to be equal to t_0, and $F(r)$ is the spatial distribution function for the delta-electron energy in the stopping medium [38]:

$$\int_{t=0}^{\infty} \int_{r=0}^{r_m} bS_e \exp\left(-\frac{(t - t_0)^2}{2t_0^2}\right) F(r) \, 2\pi r \, dr \, dt = S_e \,,$$

$$F(r) = \frac{1}{2\pi r \lambda_w(E)} \exp\left(-\frac{r}{\lambda_w(E)}\right), \qquad (3.6)$$

where r_m is the maximum value of the projection of the electron free path on the direction perpendicular to the ion path, and λ_w is a parameter determined by fitting $F(r)$ to the real expression and, therefore, is highly dependent on the energy E of the incident ion, with the result that $F(r)$ also depends on E. For instance, about 70% of the energy imparted to the electron subsystem is concentrated within a region with a radius of 0.2 nm for the case of a C$_{60}$ ion cluster with an energy of 0.025 MeV a.m.u.$^{-1}$, and within regions with radii of 5 and 12 nm for ions of Pb^{208} with energies of 3 and 20 MeV a.m.u.$^{-1}$, respectively.

In the theory of a free electron gas, the electronic specific heat of metals at low values of T_e is given by a linear function $C_e = (\pi^2 k_B^2 n_e/2\varepsilon_F) T_e$, where m_e is the electron mass, n_e is the electron number density, k_B is the Boltzmann constant, and $\varepsilon_F = (\hbar^2/2m_e)(3\pi^2/n_e)^{2/3}$. The specific heat capacity is described by this linear function up to $T_e = T_F$, where $T_F = \varepsilon_F/k_B$, while for $T_e > T_F$ it becomes a constant, namely $C_e = (3/2) k_B n_e$.

The electron heat conductivity $K_e(T_e)$ can be determined by normalizing it according to the experimental data on thermal diffusion $D_e(T_e)$ of gold, whose electrons behave like those of a quasi-free electron gas: $K_e(T_e) = C_e(T_e) D_e(T_e)$. For such metals as Ti and Zr, $D_e = 150$ cm^2 s^{-1} at $T_e = 300$ K, and $D_{min} = 4$ cm^2 s^{-1}.

The electron–phonon coupling constant g is a free parameter which can be expressed in terms of the other parameters. If the lattice temperature is not much lower than the Debye temperature T_D, the coupling constant can be approximately written as in Ref. [28]:

$$g = \frac{\pi^2 m_e n_e v^2}{b \tau_e(T_e) T_e} \,,$$

where $\tau_e(T_e)$ is the mean free time between two collisions of an electron at the temperature T_e, and v is the speed of sound in a metal, which is related to the Debye temperature T_D and the atomic number density N_a by the formula

$$v = \frac{k_B T_D}{\hbar (6\pi^2 N_a)^{1/3}} \ .$$

Finding τ_e constitutes a complicated problem [39]. As a first approximation, we can take into account the relation between $\tau_e(T_e)$ and the metal's heat conductivity $K_a(T_a)$ measured under ionic bombardment [37]. Then, assuming that the electron–phonon coupling constant is governed by the lattice temperature [37], we obtain

$$g = \frac{\pi^2 (k_B n_e v)^2}{18 K_a(T_a)} \ . \tag{3.7}$$

Equation (3.7) implies that the number density n_e of the electrons participating in conduction now becomes a free parameter. The electron number density is determined by the formula $n_e = Z N_a$, where the parameter Z for, e.g., Ti and Zr is equal to the number of valence electrons, $Z = 2$, while for Fe and Bi, according to the data of femtosecond laser experiments [40], $Z = 1.1$ and 1.3, respectively. Metals with $Z = 2$ and $\chi < 1$ (alkaline, noble, and some heavy metals) are, in relation to defect formation, only slightly sensitive to high-energy ion beams, while metals with $Z = 1$ and $\chi > 1$ (Be, Sc, Ti, V, Cr, Mn, Ge, and Re) are sensitive to such beams.

Thus, using the above approach, we can determine all the necessary parameters and coefficients of the system of equations (3.4) that are needed in order to perform calculations in the thermal spike model. The numerical solution of equations (3.4) makes it possible to evaluate the radii of the melt areas (tracks) surrounding the ion paths, and the dependence of the track size on the ion velocity for equal values of $(dE/dx)_e$, as well as to estimate the density of the energy released in the excited region for equal values of $(dE/dx)_e$.

For instance, Wang et al. [13] discovered through experiments the dependence of the track radius on the ion velocity at equal values of $(dE/dx)_e$ for Xe, Kr, and Pb ions. Apparently, for equal values of $(dE/dx)_e$ the ion velocity also plays an important role in track formation in metals that are sensitive to dense electronic excitations. Dunlop et al. [12] used the example of irradiation of titanium targets by monatomic beams and C_{60} cluster ions with approximately equal values of $(dE/dx)_e$ to show that the damaged areas have a much larger diameter around the paths of cluster ions compared to that of similar areas around the paths of monatomic ions. The outlined difference is due to the larger spatial localization of the energy released in the stopping of a cluster ion. The released energy density is related to the maximum range of delta electrons being excited. When titanium is irradiated with $1-5$-GeV Pb or U ions, the radial range of the delta electrons amounts to more than 1000 nm, while with fullerene ions the radial range decreases to several interatomic distances, with the released energy density reaching values as high as $(3-8)\times 10^2$ eV per atom.

Nevertheless, as noted earlier, such a description can be considered appropriate only for metals with a perfect crystal lattice. If the crystal structure has defects, the cross section of the energy track is determined by the characteristic sizes of the structural elements, such as the grains in a polycrystalline target or interphase boundaries (if their size is smaller than the track radius). Many experimental results concerning the effectiveness of inelastic sputtering of fine-grained metallic targets [41] corroborate this idea. When gold targets were irradiated by uranium ions with $E > 1$ GeV, the measured sputtering yield was found to be more than 10 times larger than the value predicted for elastic processes. If the energy in the electron subsystem is concentrated within a certain area of the crystal, the lattice may become strongly heated and the target could even be destroyed. The electron–phonon relaxation time is also highly dependent on other microdefects of the structure, such as impurities (in semiconductors), dislocations, microtwins, and so forth.

The characteristic relaxation times τ_{ee} and τ_{ei} for metals and semiconductors differ substantially (Table 2), which speaks for the distinction in the processes of track formation in them. According to the calculations done in Ref. [39], the relaxation times also depend on the energy spectrum of the electronic excitations (see Table 2) and the metal conduction. The rate at which the excited electrons loose their energy through scattering on phonons and on other electrons may be related to the characteristic relaxation time in energy, τ_E, in the following manner:

$$\frac{d\Delta E}{dt} = \frac{\Delta E - \Delta E^*}{\tau_E} \ , \tag{3.8}$$

where E^* is a quantity of order $k_B T$. In semiconductors, the energy imparted to the electron subsystem over a time of order τ_{ei} is transferred to the lattice, while in metals the prevailing channel of energy redistribution is electron collisions.

Table 2. Characteristic relaxation times for Si and Al [39].

ΔE, eV	0.1	0.5	1	3
τ_{ei}, s	9.4×10^{-11}	4.2×10^{-11}	3×10^{-11}	1.6×10^{-11}
τ_{ee}, s	8×10^{-10}	8×10^{-9}	2.2×10^{-8}	1.1×10^{-7}
$\dfrac{(d\Delta E/dt)_{ei}}{(d\Delta E/dt)_{ee}}$	8.5	190.4	733.3	6470.6
τ_{ei}, s	8.8×10^{-13}	4.78×10^{-13}	10^{-11}	3.74×10^{-11}
τ_{ee}, s	4.2×10^{-12}	1.7×10^{-13}	4.3×10^{-14}	5.2×10^{-15}
$\dfrac{(d\Delta E/dt)_{ei}}{(d\Delta E/dt)_{ee}}$	4.8	3.6×10^{-2}	4.3×10^{-3}	1.4×10^{-4}

Toulemonde et al. [42] used the model of a thermal spike and a melted track region to explain defect formation (using the results of measurements of electrical resistivity in the course of irradiation) in the amorphous $\alpha - Fe_{85}B_{15}$ metal alloy.

In the thermal spike approximation, the track structure after complete thermalization of the excited region depends on the type of material (type of bonds), type of lattice, target temperature during irradiation and investigations (the temperature determines the mobility of point defects), the possibility of allotropic phases appearing in the system, and the ratio of the volumes of the material in question in liquid and solid states. Similar dependences are observed in low-energy implantation of heavy ions [43, 44]. As in irradiation of materials by slow heavy ions, unusual phases can form in the case of intense electronic excitations in ion tracks. For instance, Dammak et al. [11] and Dunlop and Lesueur [27]

reported on a phase transformation in irradiated titanium targets in which the hexagonal close-packed α-phase of titanium is transformed into a hexagonal α-phase usually present at high pressures. The semimetal bismuth is of interest in this respect, since its density in the solid state is lower than in the liquid state. A local rise in pressure will cause the melting point to drop.

This can explain the results of Dammak et al. [11] and Paumier et al. [45] concerning the irradiation of bismuth crystals by highly energetic ions of O, Mg, Kr, Xe, Pb, and U at $T = 10$ K with $(dE/dx)_e$ varying from approximately 1 to 50 keV nm^{-1}. The resistivity Δc of crystals for $(dE/dx)_e > 20$ keV nm^{-1} rapidly grows already at fluences of order 10^{11} cm^{-2}. The value of Δc obtained in the case of bismuth irradiated by uranium ions with $(dE/dx)_e \approx 50$ keV nm^{-1} was found to exceed a similar value for electron irradiation by a factor of 150. Such a phase with exceptionally high electrical resistivity forms as a result of condensation of bismuth vapor on cold substrates and is similar to the phase produced under high pressures. As the phase that is formed at high pressures, the implantation phase possesses a very high resistivity and a high annealing temperature ($T > 150$ K). On the basis of these results, Dammak et al. [11] and Paumier et al. [45] inferred that each ion of Pb or U creates along its path a cylinder ($r = 20$ nm) of transformed bismuth. When these cylinders begin to unite, the entire volume of bismuth is transformed and acquires high resistivity. It is assumed that the material in such a cylinder first melts, then goes through the quenching stage under rapid cooling, and finally recrystallizes into the same phase that is produced in vapor condensation on a cold substrate.

Generally, metals for which high-pressure phases are characteristic in the pressure vs. temperature state diagram exhibit such phases in track regions under irradiation by superhigh-energy ions with $(dE/dx)_e > (dE/dx)_{thr.ph.tr}$, where $(dE/dx)_{thr.ph.tr}$ are the threshold energy losses for the phase transition.

A common way of explaining the formation of such phases is to use the ideas of shock wave generation [11, 29, 46–48] and collective atomic motion [49]. Pronounced thermal spikes near an ion path lead, among other things, to generation of thermoelastic stresses which, according to rough estimates given by Davydov and Kalinichenko [29], may exceed the strength of the material and in combination with the thermal spikes have a strong effect on the processes of defect formation, creep, diffusion, etc. With the help of the thermodynamic fluctuation theory of Davydov and Kalinichenko [29], numerical estimates have been made of the destruction of various materials caused by thermoelastic stresses that develop coincidentally with thermal spikes. The materials were divided into groups according to their electrical conductivity.

The acoustic pulses generated by particles stimulate the crystal lattice transformation and may manifest themselves far from the ion path (the long-range effect).

Several mechanisms of track formation have been discussed in the literature:

(1) the mechanism known as the Coulomb explosion [50, 51], which is effective when the ion velocity is close to the velocity of the electrons belonging to the K-shell of the target atoms, may be responsible for track formation in light targets (LiF, plastic, diamond, cubic boron nitride, etc.). A moving ion creates in the target a highly ionized cylindrical medium which is unstable because of Coulomb repulsion between electrostatic like charges (ion cores). Several related models have been formulated on the basis of this mechanism: the model of the plasma core of the track region [52, 53], the shock-wave model [46], and the model of a modified lattice potential [54]. The Coulomb explosion mechanism is also often used to explain track formation in metals and alloys [11, 16], which can hardly be justified because of the high rate of neutralization of the uncompensated charge by free electrons;

(2) the high ionization density substantially lowers the threshold energy E_d of the atomic displacements from lattice sites. The low values of E_d increase the displacement probability of the matrix atoms that receive a small amount of elastic energy from a moving ion;

(3) the thermal spike mechanism described in this section is the most often used mechanism. Within such an approach it is assumed that the energy is transferred from the electron subsystem being excited to the lattice through electron–phonon interactions [55].

Until recently the production of defects at the expense of electronic excitations in massive metal specimens was assumed to be unrealistic. Applying track-formation models valid for insulators to metals seems unjustified because of the high mobility of conduction electrons which effectively 'disseminate' the energy imparted to the electron subsystem over a larger volume and also effectively screen the ionized atoms in the ion 'tail'. So far there is no exact theory that would explain defect formation by high-energy heavy ions in metals.

The thermal spike model has been successfully used to explain track formation and to estimate the track radius in amorphous alloys with metallic conduction [16, 42]. Lately, an attempt has been made (see Refs [56, 57]) to estimate the validity range of the thermal spike model more exactly and to determine the radius of the excited region and the fraction of the energy of this region that is carried away by the pressure wave (acoustic wave) within the framework of the molecular dynamics method. However, so far numerical calculations have been done only for model materials, such as solids consisting of gases that have condensed at low temperatures. Acoustic waves may carry away up to 30–40% of the total released energy from the excited region.

The first tracks in metallic massive materials were observed in intermetallic alloys (amorphous regions). The first class consists of materials that have a complex composition and easily become amorphous because of elastic collisions when irradiated by low-energy ions or electrons [43]. Representatives of this class are characterized by low local crystal symmetry. Among such materials, NiZr$_2$, NiTi, and Ni$_3$B are especially interesting from the viewpoint of applications. In contrast to Ni$_3$B and NiZr$_2$, which have, respectively, an orthorhombic and tetragonal crystal structure in the entire temperature range, NiTi undergoes a martensite transformation at a temperature close to 300 K, is in the cubic B2 phase at $T > 300$ K, and is in the monoclinic phase at temperatures below the phase transition temperature.

The second class consists of materials with high local symmetry (LI$_2$ crystal structures). It includes the Zr$_3$Al alloy, which does not easily become amorphous as a result of elastic collisions, and the Cu$_3$Al alloy, which never becomes amorphous but may undergo chemical disordering when subjected to low-temperature irradiation in the elastic collisions mode. The classes of various intermetallic phases that become amorphous and remain stable under irradiation are listed in Ref. [43]. Here are the additional criteria that are

helpful in the prediction of whether an intermetallic alloy becomes amorphous in the elastic-collisions and intense-electronic-excitations modes: the simultaneous existence of several phases on the concentration vs. temperature state diagram; a narrow homogeneity region that allows for slight deviations from stoichiometry, and a target temperature that determines the mobility of the structure defects and their interaction (the defect kinetics). A certain correlation has been observed between the well-known experimental data on the amorphization of alloys by the method of vapor-phase deposition onto a cold substrate and by ion irradiation [43, 58].

The threshold specific energy losses for track formation in monatomic metals and intermetallic alloys amount to about 40 keV nm^{-1}, which is 4 to 10 times higher than in the case of insulators [16, 58].

Latent tracks have been observed in NiZr$_2$ at 80 and 300 K by Barbu et al. [25] and Dunlop et al. [59], who used the electron microscopy method after the specimens were irradiated by ions with $E > 1$ GeV and fluences higher than 10^{11} cm^{-2} and sufficiently large values of $(dE/dx)_e$. Irradiation by xenon ions with $(dE/dx)_e \approx 30$ keV nm^{-1} does not lead to formation of a contrast of latent tracks in the irradiated specimens, while irradiation by Pb ions with $(dE/dx)_e \approx 40$ keV nm^{-1} provides a picture of passage from discontinuous to quasi-continuous tracks. Uranium ions with $(dE/dx)_e \approx 54$ keV nm^{-1} form tracks that are, for all practical purposes, continuous. The number of tracks per unit specimen area correspond exactly to the number of incident ions. Electron diffraction data suggest that there is an amorphous material inside the cylindrical disturbed region within the ion path. Closely related results were obtained somewhat later by Barbu et al. [58], when the Ni$_3$B compound was irradiated by ions with a high level of $(dE/dx)_e$. However, in this case the tracks were found to be unstable at room temperature. No visible tracks in this compound were detected several months after ion irradiation.

What is interesting from the scientific and application angles is the phase transformations in NiTi which is one of the alloys with thermomechanical shape memory (a thermoelastic transformation near room temperature). In examining the possibility of such transformations we arrive at two possible courses that such phase transformations may take:

(a) a martensite transition in NiTi from the low-temperature (80 K) monoclinic structure to a high-temperature cubic structure in accordance with the thermomechanical actions, and

(b) phase transformations as functions of the irradiation temperature (irradiation may be done at a temperature at which the target contains either only one phase or both phases).

The main results of the studies conducted by Barbu et al. [16, 58–60] is that the sensitivity of cubic and monoclinic phases to electronic excitations is different. Above the threshold value of $(dE/dx)_e \approx 48$ keV nm^{-1}, the tracks in the NiTi alloy exist only in those areas of the specimen that were in the monoclinic phase during ion implantation. Figure 2a shows the electron micrograph of a specimen in which both phases existed during ion irradiation. The tracks are observed in the monoclinic interlayer and are not present in the surrounding cubic matrix. Figure 3 clearly shows amorphous tracks that were observed in the cubic phase of the NiTi specimen irradiated by uranium ions (prior to irradiation the specimen was in the monoclinic phase). The
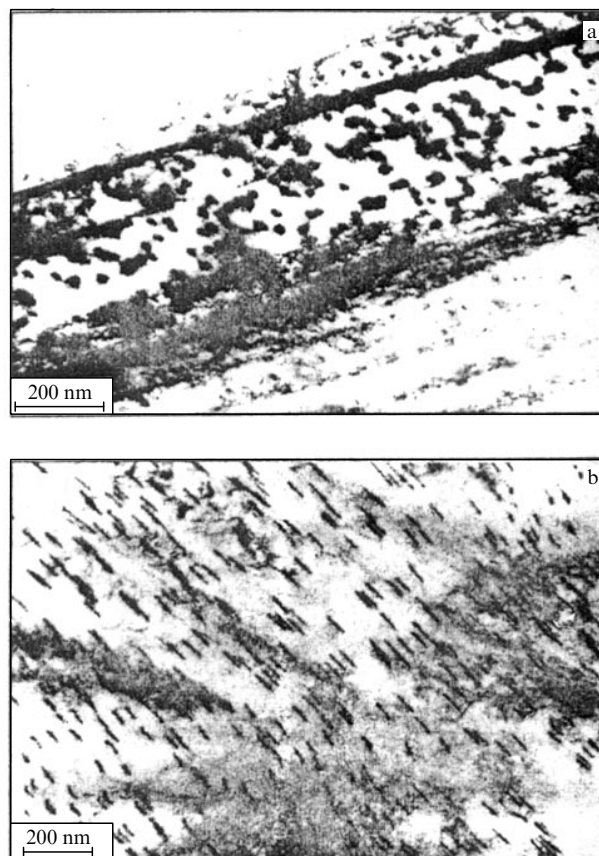
Figure 2. Bright-field electron micrographs of (a) an NiTi specimen irradiated at $T = 300$ K by Pb ions with $E = 0.84$ GeV, $(dE/dx)_e \approx 52$ keV nm^{-1}, and a fluence of 10^{11} cm^{-2} [58], and (b) a monoclinic NiTi specimen irradiated at $T = 80$ K by uranium ions with $E = 0.76$ GeV, $(dE/dx)_e \approx 57$ keV nm^{-1}, and a fluence of 5×10^{10} cm^{-2} (the micrograph was taken at $T = 300$ K). The latent tracks are evident in Fig. 2a only in the monoclinic lattice but not in the surrounding matrix, the latter being in the cubic phase during irradiation.

tracks created in the low-temperature phase are clearly apparent; they have a diameter of 12 nm and are homogeneously distorted cylindrical regions. According to electron diffraction data, they are amorphous and remain stable when the specimen transforms back into its cubic structural modification at an alloy temperature of 300 K.

The presence of a substantial number of amorphous tracks does not hinder phase transformations. The structural stability of the tracks is very obvious, since there occurs a certain displacement during the phase transition. This manifests itself in a clear-cut slant of the tracks. Figure 2b corresponds to a specimen that was irradiated in the monoclinic phase at 80 K; here, the tracks appear over the entire specimen. If the specimen is subsequently heated to room temperature, its material transforms into the cubic modification. In this transformation, the monoclinic interlayers turn by several degrees in relation to each other. At the temperature at which the microscopic study was conducted, the matrix was entirely in the cubic modification. The amorphous tracks appear to be slightly disoriented due to the memory effect. When the specimen is returned to its monoclinic phase by lowering the temperature, the initial orientation of the tracks is restored. Here the tracks serve as markers of the displacing phase transition.
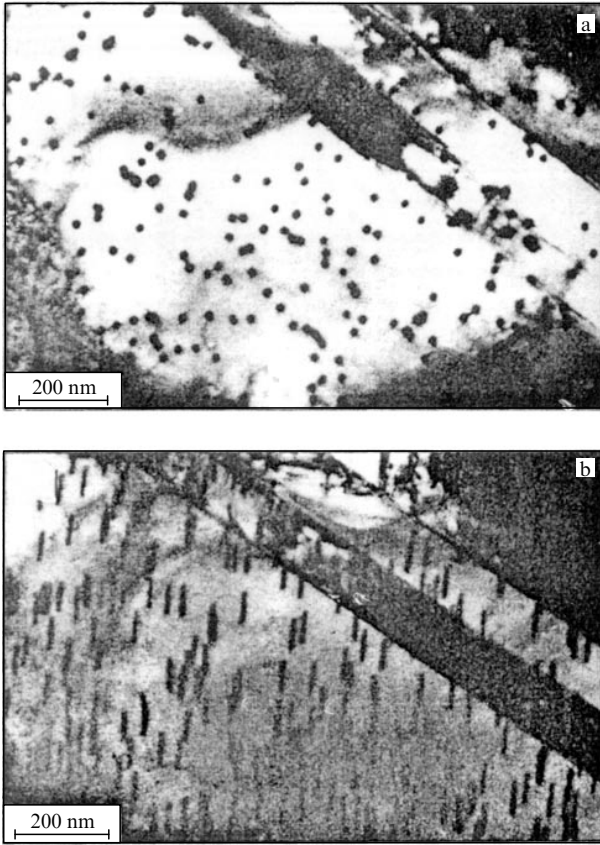
Figure 3. Bright-field electron micrographs of a monoclinic NiTi specimen irradiated at $T = 90$ K by uranium ions with $E = 0.76$ GeV, $(dE/dx)_e \approx 57$ keV nm^{-1}, and a fluence of 5×10^{10} cm^{-2} [58]. At $T = 300$ K, the amorphous latent tracks are clearly visible. (a) The electron beam is parallel to the ion beam. (b) The specimen is turned in the microscope through an angle of $27°$.

4. Effects accompanying the passage of high-energy ions through metals

4.1 Inelastic metal sputtering

When swift ions interact with condensed matter, the surface of material may become eroded because of an intense excitation of the electron subsystem; this phenomenon is known as inelastic sputtering. The studies conducted by Baranov et al. [61] in respect to the bombardment of metals as well as oxides and fluorides of the metals by fission fragments and swift ions have shown that inelastic sputtering differs from ordinary sputtering by its laws and physical mechanisms. The inelastic sputtering yield may exceed the values characteristic of elastic sputtering by a factor of ten or more. For instance, Lapteva and Ershler [62], who were the first to discover inelastic sputtering, found that the sputtering yields of uranium and plutonium by fission fragments exceed the expected values by a factor of 10 to 100.

The distinction in the mechanisms of elastic and inelastic sputtering determines the distinction in the dependences of the corresponding sputtering yields S on the ion energy and on $(dE/dx)_e$. The energy dependence of the inelastic sputtering yield $S(E)$ on the whole follows the energy dependence of the inelastic losses $(dE/dx)_e$, with $S \sim (dE/dx)_e^n$, where $n = 2 - 4$.
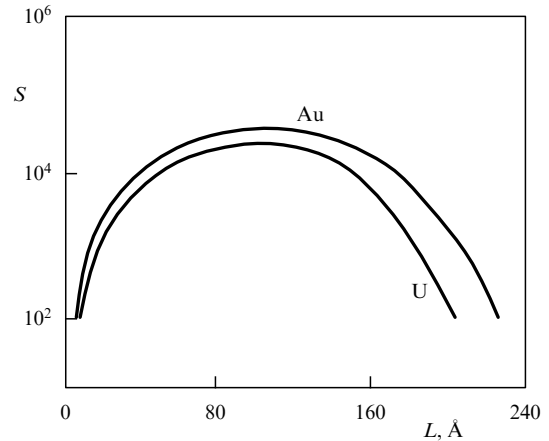

Figure 4. Inelastic sputtering yield S of Au and U targets by fission fragments with $Z_1 \approx 50$ and $E \approx 100$ MeV as a function of the average grain size L [61].

The results of the experimental research done by Lapteva and Ershler [62] and Birtcher et al. [63] suggest that inelastic sputtering, at least for metals and metal oxides, occurs only when the target surface is an ultradispersive layer with a grain size $L \leqslant 30$ nm (Fig. 4), and the electronic stopping power of the material is no lower than $6 - 30$ keV nm^{-1} (there is a threshold for a certain grain size). Characteristically, inelastic sputtering for fine-grained metals with grain sizes $L \leqslant 10$ nm (see Fig. 4) is 10 to 1000 times larger than for coarse-grained materials [62 – 64]. If the surface layer of the material has a coarse-grained structure, then $S \sim S_n = 1/N \; (dE/dx)_n$, where $(dE/dx)_n$ are the nuclear energy losses of the ions, with the result that sputtering proceeds by the elastic mechanism ($S \leqslant 10$ atoms per ion). In inelastic sputtering, the sputtering yield is, as noted earlier, proportional to the electronic stopping power and hence increases with the ion energy (Fig. 5) in the energy range where $(dE/dx)_e \sim E^n$. Usually, either of two models is used to explain the available results: the isolated grain model or the model of 'free hot

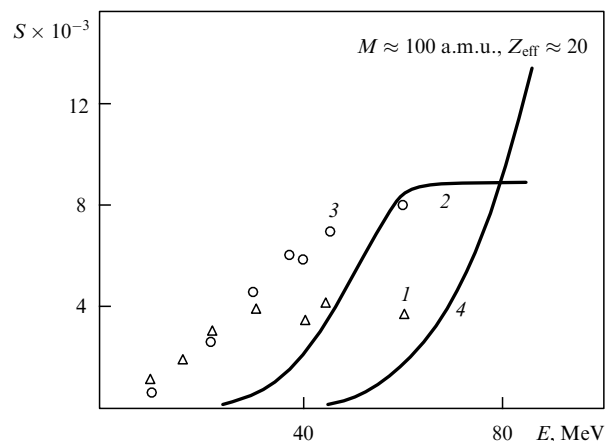**Figure 5.** Energy dependences of the sputtering yield of fine-grained gold layers by fission fragments [63]: *1* — experimental data with the average grain size $L \approx 3$ nm, *2* — results of model calculations by Birtcher et al. [63] for grains with $L \approx 3$ nm, *3* — experimental data for targets with $L \approx 7.5$ nm, and *4* — results of calculations by Birtcher et al. [63] for grains with $L \approx 7.5$ nm.

electrons on the grain boundaries of the metal'. In the first approach [61] it is assumed that all the energy imparted by an impinging ion to the electron subsystem of a grain proves to be 'locked inside' the grain and is utilized to heat and evaporate the grain. The isolated-grain model can be used when small singular grains have a small area of contact with the metallic substrate or lie on an insulating substrate.

In the model developed by Martynenko and Yavlinskiĭ [41], when an ion flies into a grain it excites electrons at a distance of roughly 1 nm from its path. After approximately 10^{-15} s, the electrons become thermalized via thermal diffusivity ($3-4$ cm^2 s^{-1}) and the hot electrons with an energy in the $1-10$ eV range become Bloch electrons (i.e., are only slightly scattered in the grain). The situation is quite special in the area where the grain is in contact with the substrate. The hot electrons, on their way from the grain to the substrate, interact with atoms as free electrons prior to the first collision. Since the mean free path of electrons with an energy of roughly 10 eV is approximately 1 nm, the atoms of the substrate and the grain that are at a distance of about 1 nm from the interface will rapidly acquire energy from the hot electrons, with the result that the substrate exerts pressure. Calculations show that the grain may tear itself away as a whole from the substrate. The proposed mechanism of energy transfer to the atoms near the grain boundaries explains why sputtering occurs predominantly along the normal to the surface [63], the presence of tracks of swift ions in fine-grained metals [50, 65], and the sintering of finely dispersed powders and thin films in the course of their irradiation by swift multicharged ions [66].

There are also other approaches to interpreting the data, namely, evaporation of single atoms from the grains, the ejection of atoms due to acceleration in the double electrical layer of a grain [63], the removal of grains through 'shaking-off' by the shock wave generated in the passage of an ion through a nonconducting substrate, and the 'bouncing' of grains caused by rapid thermal expansion [67].

Recent experiments conducted by Didyk et al. [68, 69] have shown that the grain boundaries of polycrystalline metals are sputtered much more intensely than the grain surface. The characteristic value of the sputtering yield S for the grain boundaries is no less than 10^3 atoms per ion. Here, as the defects accumulate in the process of irradiation of nickel by krypton ions with $E = 305$ MeV up to a fluence of 3×10^{15} cm^{-2}, the metal sputtering yield on the grain surface rapidly grows and becomes comparable to the grain-boundary sputtering yield. The explanation is that, as the defects accumulate in the crystal, the electron–phonon relaxation times get shorter, hot tracks form, and the evaporation sputtering mechanism comes into action. The value of S becomes comparable to the amorphsized-metal sputtering yield [70].

4.2 Plastic deformation, creep, and growth
A second interesting effect that has recently been discovered is that the size of the layers of amorphous metal alloys increases in the directions perpendicular to the ion beam and that the layer thickness decreases in the process, with the volume remaining practically unchanged (Figs 6 and 7).

Thus, there occurs a considerable displacement of material, just as in the rolling of foil or applying a sledgehammer to the foil. Here are the main peculiarities of this process [72–79]. The effect is observed in metal alloys (Ni$_3$N, Pd$_{80}$Si$_{20}$, Fe$_{85}$B$_{15}$, and Ti$_{50}$Be$_{40}$Zr$_{10}$), insulators
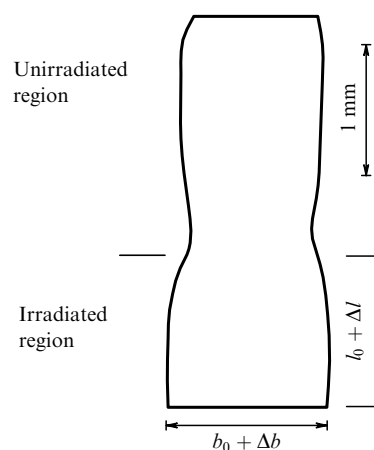

Figure 6. Schematic of the effect of the plastic flow of amorphous materials under ion irradiation. Here, b_0 and l_0 are the initial transverse and longitudinal dimensions of the specimen, and Δb and Δl are the increments of the quantities, respectively, acquired under irradiation.
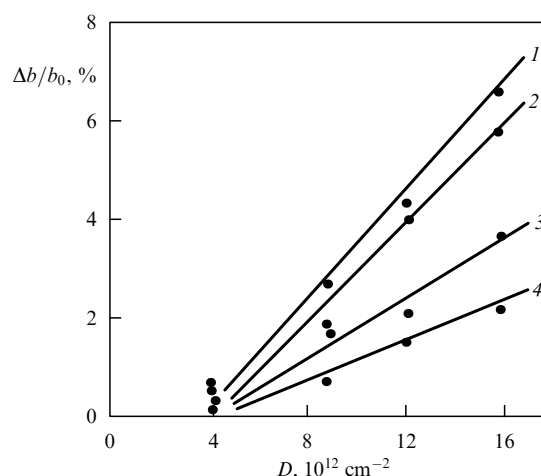

Figure 7. Variation of the transverse size of specimens of a cold-rolled film of the amorphous Pd$_{80}$Si$_{20}$ alloy bombarded by Xe$^+$ ions with $E = 1.34$ MeV a.m.u.$^{-1}$ as a function of the ion fluence [71] for the following film-thickness values: 1 — $b_0 = 2$ μm, 2 — $b_0 = 4.5$ μm, 3 — $b_0 = 7$ μm, and 4 — $b_0 = 8.1$ μm.

(SiO$_2$), and semiconductors, provided they are in an amorphous state. The effect becomes more evident at higher values of the electronic stopping power and at lower irradiation temperature. For the Fe$_{85}$B$_{15}$ alloy it was found that plastic deformation is not annealed even at room temperature. The effect cannot be saturated. Most often there is an incubation radiation fluence before plastic deformation of a material sets in. As long as this fluence is not reached, defects accumulate, as observed in resistometric experiments. When external tensile stresses are applied, the effect is enhanced significantly, while compression stress suppresses the effect. Placing relatively thick marker layers of gold 20- and 100-nm thick between two amorphous layers of Ni$_2$B, each 1.5-μm thick, did not result in a noticeable change in the plastic deformation process in either case. The rough surface of glass-like materials becomes smoother (mirrorlike) as a result of the plastic flow of the material, caused by ionic bombardment.

Placing crystal layers of Au and W 20-to-900-nm thick between thick amorphous glassy metals made of Ni$_3$B (1 –

1.5 μm) [76, 78] and irradiating this wafer by Ti^{22+} ions with $E = 500$ MeV results in radiation-induced creep setting in the crystal layers. The effect is not observed with free crystalline materials. Here, the variation of the thickness of the metal layer is due not to the penetration of ions through the film but to the plastic deformation occurring in the adjacent amorphous layers. By measuring the variation of the metal film thickness we can find the stresses generated by a beam of swift heavy ions passing through the amorphous solid, which were estimated at 2 GPa [76, 78].

The above effect is closely related to the rapid increase in the electrical resistance R when the threshold fluence is reached [72]. Just like plastic deformation, the new effect strongly depends on $(dE/dx)_e$ (Fig. 8) [there is a threshold value of $(dE/dx)_{e, thr}$]. For low irradiation fluences (up to the incubation level), the ratio $\Delta R/R_0$ (where R_0 is the resistance prior to irradiation, and $\Delta R = R - R_0$) is independent of the direction of irradiation (the angle φ between the direction of the ion beam and the normal to the target). After the end of the incubation period, $\Delta R/R_0$ obeys the following law [72]:

$$\frac{\Delta R(\varphi)}{R_0} = \frac{\Delta \rho}{\rho_0} + \frac{2\Delta x(\varphi = 0)}{x_0} \left(1 - 3\sin^2 \varphi\right),$$

where ρ and ρ_0 are the current and initial resistivities of the specimen, respectively, with $\Delta\rho = \rho - \rho_0$, and x and x_0 are the current and initial sizes of the specimen along the direction of the ion beam, respectively, with $\Delta x = x - x_0$. A similar dependence of the plastic flow of the material on the irradiation angle has also been observed in experiments by Benyagoub and Klaumunzer [73].

There is as of yet no rigorous theoretical model that describes all these processes. We must assume that the amorphous material acts as follows: (a) it provides sufficient

free volume for substantial mass transfer to be possible, and (b) it drives the electron – phonon interaction time down in the relaxation stage for the excited region. The most favorable pattern of track formation for the development of strong tangential stresses is the one in which a hollow region (or a region with reduced atomic density) forms in the track core, with the region surrounded by a shell with a large number of implanted interstitial atoms. Such shells generate high stresses. As the fluences increase, the number of such track regions grows (and so do the stresses) up to the point where they cover all the surface of the specimen (incubation period). Knowing the incubation fluence D_{inc} found through experiments, we can calculate the size R_{tr} of the track:

$$D_{inc} = \frac{1}{\pi R_{tr}^2}.$$

For instance, for 3-GeV Xe ions bombarding the $Fe_{85}B_{15}$ alloy [73], $D_{inc} \approx 5 \times 10^{12}$ cm^{-2}, which yields $R_{tr} \approx 2.5$ nm. At low irradiation temperatures, the vacancies are immobile and defect annealing is inhibited. Longitudinal stresses effectively relax on the specimen surface, while tangential stresses may relax only under subsequent irradiation. Under such irradiation, the target ions that land into formed track regions act as triggers for mass diffusion of atoms in the transverse direction under tangential shear, i.e., plastic flow of the material begins. This explains the dependence of $\Delta R/R_0$ and the size of the deformation on the orientation of the target in relation to the ion beam. Additional tensile stresses applied do not change the incubation fluence: they only enhance the effect when $D > D_{inc}$.

The above hypothesis was proposed in Ref. [80]. Lately, in a number of works (e.g., see Refs [81–86]) the anisotropic increase of the transverse size of specimens and the relaxation of stresses in amorphous materials, both induced by ion irradiation, have been described in terms of viscous flow and the relaxation of shear stresses in locally heated, disturbed regions near ion paths. In such a semiquantitative theory, local heating is caused by intense electronic excitations. In materials with a strong dependence of viscosity on the temperature and the defect concentration (as in amorphous alloys), a rapid increase in temperature and defect concentration leads to a radical reduction in viscosity within a small volume of the material near the path of a swift heavy ion, and this reduction happens in a very short time: $t \sim t_{ei} \sim 10^{-11} - 10^{-12}$ s. Hence, large temperature gradients, displacements of the primary atoms, and the momenta of the primary atoms near an ion path may be the reason for plastic flow in the material in the direction perpendicular to the ion beam. The elastic energy stored in the track contributes significantly to the driving force of track etching.

The presence of threshold values of $(dE/dx)_{e, thr}$ for stress relaxation and anisotropic growth is stipulated by the need for a sufficiently distinct thermal spike to form, i.e., a fairly high local temperature must hold for a fairly long time. The duration of the incubation period (the incubation irradiation fluence) reflects the rate at which the viscosity of the amorphous material decreases. It can be more or less prolonged for small values of $(dE/dx)_e$ and diminishes or disappears entirely as $(dE/dx)_e$ increases. Stress relaxation enhances with target temperature, but the rate of anisotropic growth decreases as the temperature grows. The stressed track regions are like a mesoscopic probe for analyzing the creep in the media surrounding the tracks.
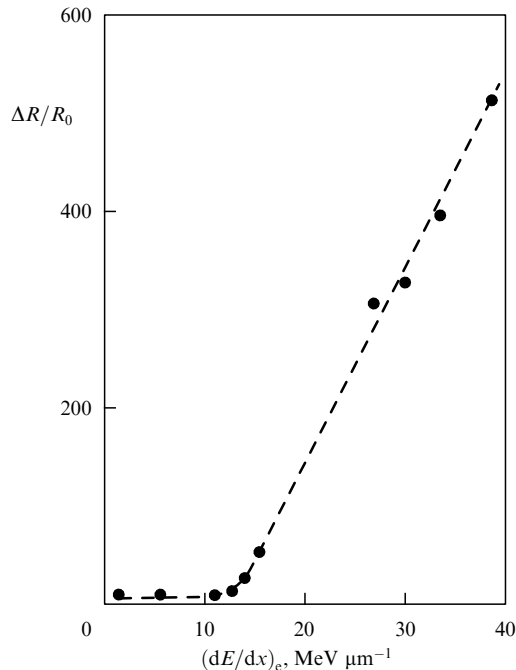

Figure 8. Relative variation of the electrical resistance of a $Fe_{85}B_{15}$ specimen as a function of the electronic stopping power $(dE/dx)_e$ (irradiation was carried out at $T = 90$ K, and the measurements at $T = 77$ K).

4.3 Other effects

Intense electronic excitations are the cause for ion-beam mixing in layer structures. Such an effect was observed in many double-layer and multilayer systems: metal–metal, metal–semiconductor [87–91], and metal–insulator [92].

The thermal spikes created by swift heavy ions may be the driving force behind the mixing of metal–ceramic material systems (Fe, Cu, Ni, Ti, Au, Ag)/(MgO, Al_2O_3, SiO_2, ZrO_2) and the increase in interphase adhesion, as in the case of thermal spikes created by atomic displacement cascades for the keV–MeV energy range [92, 93].

High-quality adhesion of metallic coatings on polymers is important for the fabrication of multilayer electronic systems and microtechnology. High cohesive strengths have been achieved (through irradiation by beams of Bi ions with $E = 0.3 - 2.6$ GeV and relatively low fluences of $10^7 - 10^{13}$ cm^{-1}) with a double-layer system consisting of a 300-nm thick copper film on a polychlorotrifluoroethylene (Teflon) substrate [94].

By high-energy implantation of 100-MeV ions of boron and phosphorus into soft-magnetic amorphous ferromagnetic alloys Fe-Cu-Nb-Si-B and Fe-B-Si-C, it is possible to achieve a high value of permeability [95]. High-energy ion implantation is also applied to increase severalfold the hardness of materials to considerable depths [96, 97] and to polish the surface of metals or to enhance the erosion of their surface [98].

5. Track formation in semiconductors

Numerous experiments on defect formation in insulators, metals, alloys, and amorphous semiconductors have shown that these materials are sensitive to track formation when they are bombarded by high-energy heavy ions. Nevertheless, the conditions of track formation and the inner structure of tracks (phase composition) in metals, insulators and semiconductors, crystalline and amorphous solids, films, and massive specimens differ substantially.

The situation becomes especially complicated when we deal with the irradiation of semiconductors by swift heavy ions. The irradiation of crystal silicon, germanium, and gallium arsenide at room temperature by swift ions, conducted at numerous accelerators all over the world, did not lead to any specific effects caused by the high intensity of electronic excitations [99–109]. Studies involving deep level transient spectroscopy (DLTS), Hall measurements, transmission spectroscopy, optical absorption measurements, electron paramagnetic resonance (EPR), and measurements of electrical resistance did not reveal new types of structural defects. The effectiveness of defect formation or defect annealing stimulated by the high level of electronic excitations depends on $(dE/dx)_e$ and ion velocity. In contrast to electron and neutron irradiation, the effectiveness of defect formation in the case of irradiation by swift heavy ions is governed by the type of semiconductor (Si, Ge, or GaAs). For instance, in germanium, on which a substantial number of experiments were carried out involving swift ions from oxygen to lead [103, 108] with $(dE/dx)_e$ varying from 5 to 35 keV nm^{-1}, no significant effects of intense electronic excitations were exposed. Vlasukova et al. [109] and Mikou et al. [110] arrived at similar conclusions in their GaAs studies. However, the effectiveness of defect formation in a silicon substrate by stopping of swift heavy ions was approximately 15 times higher than for electrons [109]. In

the case of neutron irradiation, no such difference has been observed. The ratio of the damage factors for neutron and electron irradiation is equal to the ratio of the cross sections of the respective elastic processes [108].

The specific energy losses $(dE/dx)_e$ for any monatomic ions in silicon do not exceed 28 keV nm^{-1}. However, recent experiments [111, 112] on irradiation of crystal silicon by fullerene ions C_{60}^{2+} with $E = 30$ MeV and $(dE/dx)_e = 48$ keV nm^{-1}, as well as with $E = 40$ MeV and $(dE/dx)_e = 57$ keV nm^{-1} revealed the formation of tracks with entrance diameters amounting to 8.4 and 10.5 nm, respectively. The track diameters remain constant down to a depth of roughly $80 - 100$ nm [111], and at larger depths gradually decrease. Very often the tracks end in a series of droplets of disturbed material along the ion paths (the discontinuous section of the tracks).

The limited depth at which tracks are observed is determined mainly by the nuclear scattering of the components of a fullerene cluster from the atoms of the stopping medium and by their separation. The total range of the cluster components amounts to about 1 μm. The second (less important) factor in the decomposition of a fullerene molecule is the Coulomb repulsion of its fragments (carbon ions) due to ionization of carbon atoms (the effective charge of the fullerene complex). The threshold values of the energy losses $(dE/dx)_e$ for track formation in Si$^+$ are roughly 30 keV nm^{-1}.

Thus, on the basis of the results of these investigations we can hypothesize that in Ge and GaAs crystals there may be tracks if the ion energy losses are higher. When semiconductors are irradiated by fullerene ions, the density of the energy released near the ion paths (over the correlation length) is very high, since the maximum ranges r_{max} of the delta electrons amount to only 1.9 and 2.7 nm for C_{60} with $E = 30$ and 40 MeV, respectively, while for an ion of ^{238}U with $E = 1$ GeV, we have $r_{max} = 1050$ nm. Hence, the entire released energy is localized near the path of the fullerene ion. This is an important factor in the description of track formation in semiconductors irradiated by ion clusters.

When silicon and germanium are irradiated by monatomic ions, tracks can be observed only if the parent material is in an amorphous or finely dispersed single-crystal state [113, 114] (recrystallization of the material along the ion paths). The investigations were made under very specific conditions: the targets were deposited films 5 nm thick with very small grains, usually 1 nm [113]. In such specimens, Au ions with an energy of 207 MeV and $(dE/dx)_e = 17$ keV nm^{-1} produce discontinuous tracks 7 nm in diameter. These results can be explained by the thermal spike model with two factors taken into account: (1) the melting point of amorphous (and, apparently, ultradispersed) silicon is reduced by $200 - 250$ K (see Section 3), and (2) at the same time the electron–phonon coupling constant increases (the electron–phonon relaxation time decreases). Track formation in the thin films of ultradispersed materials is also stimulated by the strong limitation, caused by the proximity of grain boundaries and surfaces, on the spreading of the released energy over the entire volume. The tracks in amorphous silicon and germanium consist of small recrystallized particles (discontinuous tracks) [114]. The threshold values of $(dE/dx)_e$ for track formation amounted to 5 keV nm^{-1} for germanium, and 15 keV nm^{-1} for silicon.

A number of researchers studying irradiation of semiconductors by swift heavy ions examined the annealing of

defects that had been produced, prior to the main irradiation, through bombardment by light ions. For instance, in single-crystal silicon there is observed the effect of strong annealing of defects that were introduced earlier by protons when irradiation was done by xenon ions with $E = 340$ MeV and a fluence of 10^{12} cm^{-2} [115]. Such removal of defects has also been registered *in situ* in single crystals of Ge, GaAs, and GaP [103, 116–118], and it correlates well with the high values of the energy imparted to the electron subsystem. At the same time, the results of Chavan et al. [119] suggest that the implantation of 90-MeV silicon ions into silicon with a fluence in the range $(1.25–5)\times10^{14}$ cm^{-2} leads to the formation of a large number of defects, and even with the highest ion fluence no trace of the effect of annealing of the created defects can be observed. Thus, processes of defect formation or defect annealing and track formation due to electronic excitations depend on the level of these excitations and the density of the energy imparted to electronic excitations near ion paths (Fig. 9).

So far, direct resolution methods have not revealed the formation of latent tracks in such wide-gap semiconductors as diamond and α-SiC. Single-crystal α-SiC specimens have been bombarded by 5.5-GeV xenon ions with fluences up to 10^{14} cm^{-2} [120]. Transmission electron microscopy has not discovered any extended defects in irradiated specimens. Nevertheless, after annealing the specimens at $T = 1373$ K it was discovered that there is a substantial number of dislocation loops. Finally, Lhermitte-Sebire et al. [121] conducted TEM studies of a complex ceramic matrix SiC$_f$–SiC irradiated at $T = 300$ K by swift xenon ions with fluences up to 10^{15} cm^{-2} and found that there were amorphous zones localized in interphase regions and also directly in the fibers. Latent tracks were also observed near the interphase boundary between a SiC$_f$ fiber and the SiC matrix.

In the works of the Belorussian scientists (Zaitsev et al. [122, 123], Varichenko et al. [124, 125], and Ertchak et al. [126]) EPR and photoluminescence were used to study the types of point defects generated by swift heavy ions in diamond and cubic boron nitride. The researchers determined the inherent role that electronic excitations play in the formation of some types of point defects, studied the combined effect of elastic and inelastic processes on the formation of simple defects and the distribution of these defects over the crystal's depth; moreover, by using the cathodoluminescence method they discovered high-pressure phases in the materials they studied. In cubic boron nitride, the high-pressure phases were detected under irradiation by ions of Ne, Co, and Xe with an energy of about 1 MeV a.m.u.$^{-1}$ [122]. The pressure was estimated from the spectral shift of the narrow phononless photoluminescence line emitted by radiation centers (RC).

The above researchers (see Refs [122–126]) used the EPR method to reveal the formation of track-like one-dimensional nontetrahedral structures (channels) along the ion paths in the event of high-energy ion irradiation. The channels possess high electrical conductivity and diffusion effectiveness for impurity atoms. The presence of implanted atoms at depths much larger than the mean projected range of ions, R_p, was related to the salient features of such track regions. It was assumed that the nanosized region near an ion path has a reduced atomic density, while the periphery has an enhanced density of matrix atoms (the high-pressure phases). The channels ensure an enhanced diffusion mobility of the impurity atoms at fairly low temperatures, i.e., temperatures not characteristic of diffusion of atoms in diamond and cubic boron nitride, and the possibility of some of the ions being trapped in such channels created in earlier stages of irradiation (long-range tails in the distribution of atoms over the depth of the crystal) [123]. The Coulomb explosion mechanism or the generation of shock waves may be responsible for channel formation.

Very illustrative and interesting are the results of Vetter et al. [127], who used a high-resolution microscopy method and found that in single-crystal GeS implanted with heavy ions with energies in the $5.9–13$-MeV a.m.u.$^{-1}$ range there were latent elliptical tracks with an amorphous core (Fig. 10). The researchers observed that around the tracks there are contrast regions related to the stresses generated in
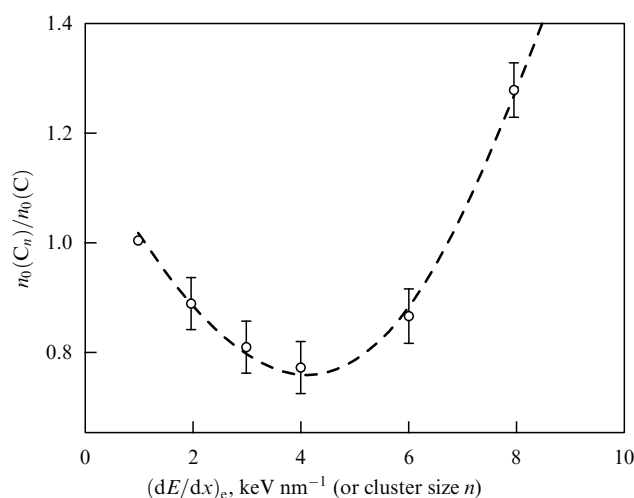
Figure 9. Evolution of the effectiveness of the defect generation per cluster as a function of the energy imparted to the electron subsystem, or as a function of n, the number of atoms comprising a cluster, in silicon irradiated by carbon clusters C$_n$ ($n = 1–8$) at a constant rate of 0.8 MeV s^{-1} [111]; n_0 is the effectiveness of the defect generation per cluster.\
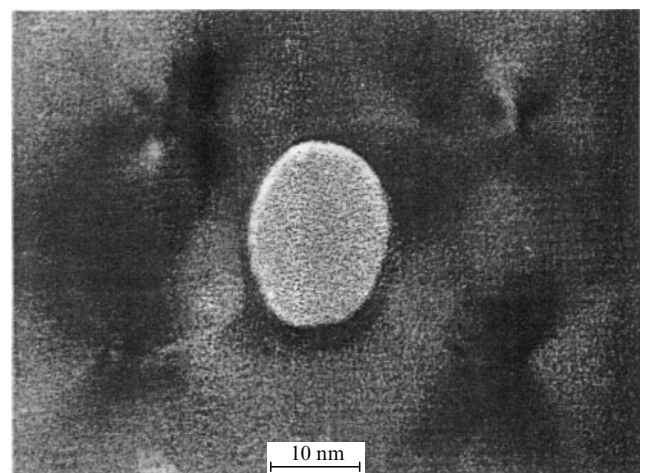
Figure 10. High-resolution electron-microscope image of a separate track in GeS, caused by the passage of a uranium ion with $E = 5.6$ MeV a.m.u.$^{-1}$ [127]. The amorphous area is 21.8×15 nm. The track is surrounded by four regions of stress contrast.
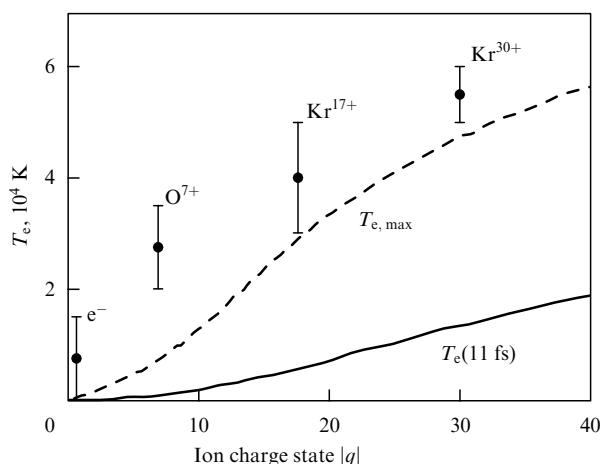
Figure 11. Experimental values of the electron temperature in amorphous carbon vs. the charge of the initial particle for a 5-MeV a.m.u.$^{-1}$ impinging ion, compared to the results of the thermal spike model [37]: • represents experimental data, the solid curve represents results of calculations done within the thermal peak model, and the dashed curve represents the estimates of the maximum temperatures given with the thermal peak model at the instant of time $t = 0$.

the surrounding matrix. The ratio of the length of the tracks along the two axes of the ellipse is 21.2 nm to 18 nm, which corresponds with the inverse ratio of the lattice constants for GeS ($a/c = 1.175$).

According to these results, a track in a wide-gap semiconductor can be interpreted as consisting of a multi-vacancy core surrounded by a shell enriched by interstitial atoms. The crystalline shell surrounding the ion track may be subjected to a strong compression stress [122, 127 – 131]. Such track geometry is extremely conducive to the formation of solid fullerenes in carbon-containing materials (diamond, graphite, and polymers) [132].

Bitensky et al. [133] were the first to present experimental results concerning the electron temperature at the center of latent tracks. These results were found on the basis of data on high-resolution spectra of Auger electrons being excited. The experimental values of the temperature were compared with results of calculations done within the scope of the thermal spike model (Fig. 11) for swift ions with $E = 5$ MeV a.m.u.$^{-1}$ in amorphous self-sustaining carbon films. These temperatures are characteristic for times of about 10 fs after a particle has passed. Figure 11 shows that the temperatures calculated using the thermal spike model are much lower than the real electron temperatures. The reason for this is either an insufficiently accurate description of the heat source as a function of time and position or the overestimation of the heat capacity of the given material in the thermal spike model.

6. Track migration of atoms and track channeling of ions

There are certain specific effects inherent in tracks in wide-gap semiconductors. Among these are the migration of impurity atoms along tracks [122] and the channeling of ions in tracks formed in earlier stages of ion implantation [123, 134]. The structure of tracks with reduced atomic density, similar to a 'tube', can be the cause of enhancement of diffusion.

As is well known, the diffusion of impurities in diamond occurs at temperatures above 2000 °C. Hence, the fact that the diffusion shows up at great distances from the specimen surface at lower temperatures can be explained by the effect of specific structures that are formed as the ions penetrate through the specimen on the enhancement of atomic mobility. This has been corroborated in experiments involving the irradiation of diamond and cubic boron nitride by swift ions [122]. The track migration effects are illustrated in Fig. 12. Here, two profiles of the depth distribution of helium atoms implanted into diamond with an energy of 300 keV (Fig. 12a) and an energy of 200 keV (Fig. 12b) and then annealed at $T = 1000\,°C$ are compared.

If the diamond specimens had been previously irradiated by xenon ions with an energy of 1 MeV a.m.u.$^{-1}$, helium atoms migrated at $T = 1000\,°C$ to a depth of 6 μm. Figure 12 shows that helium migration is effective only in track-containing layers, since helium atoms do not reach the depths where a layer of the material springs up that contains the implanted xenon atoms and is rich in defects. The first peak in the depth distribution profile of helium characterizes the initial distribution of implanted helium, while the second peak corresponds to the distribution of the helium atoms trapped in tracks and then migrating along the tracks. The track migration mechanism can be used to explain the fact that the distribution of xenon atoms has a long 'tail' directed to the surface, when irradiation was carried out at 1350 °C. But if the irradiation of the specimens by xenon ions had been
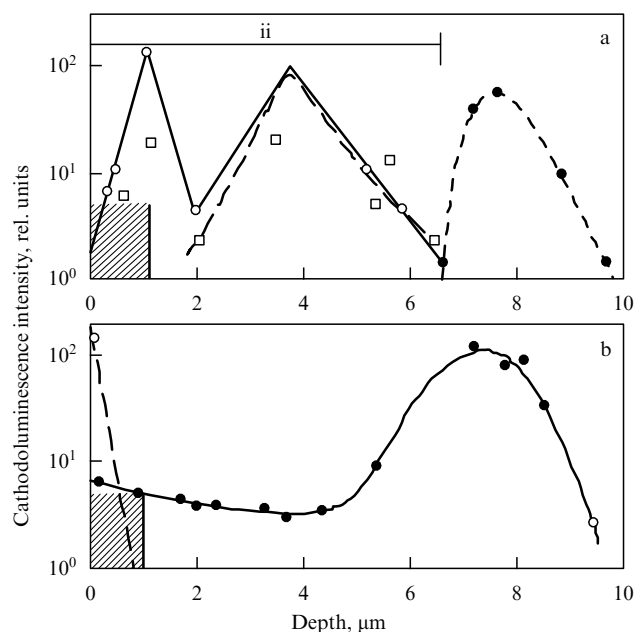

Figure 12. Track migration in diamond irradiated by Xe^{+} ions with energy $E = 124$ MeV. Depicted are depth distributions of helium-containing centers with $\lambda = 536.5$ nm (o) and with $\lambda = 560.5$ nm (□), and xenon-containing centers with $\lambda = 816$ nm (•) recorded by the cathodoluminescence method for the following specimens: (a) irradiated at room temperature by xenon ions and then by helium ions with $E = 300$ keV with subsequent annealing at $T = 1000$ °C, and (b) irradiated at $T = 1350$ °C by Xe^{+} ions and then at room temperature by helium ions with $E = 200$ keV with subsequent annealing at $T = 1000$ °C. The ii layer contains tracks. The dashed curve represents the results of theoretical calculations for the layer containing implanted helium, and the hatched area represents the layer which contains implanted helium for the case without previous ion irradiation.

carried out at room temperature, subsequent thermal treatment did not lead to a redistribution of xenon atoms belonging to the ion-implanted layer. Zaitsev [122] assumed that some of the xenon atoms implanted into the heated lattice do not have enough time to find stable positions for themselves and, hence, migrate along the tracks to the specimen surface.

On the basis of the research into radiation-stimulated diffusion of impurities in single-crystal silicon and diamond [122, 135] one would be inclined to conclude that after a swift heavy ion has passed through the specimen there forms a destructurized region (a track) along which impurity diffusion may proceed. This fact is important for applications, since it makes it possible to implant impurities after irradiation by heavy ions via ordinary diffusion processes at elevated temperatures. Here, the packing density of doped nanosized cylindrical regions reaches 10^{12} cm^{-2}. This approach may serve as a rough idea of what track nanoelectronics for electronic and optoelectronic devices may be like.

Another possible corroboration of the track formation caused by high-energy ion implantation may be the effect of deep penetration of some of the ions (trapped in earlier created tracks) within the specimen. Indeed, it is difficult to imagine that channels with reduced atomic density (in some materials these channels are almost entirely hollow) have no influence on the passage of swift ions, especially if the channels are oriented strictly along the direction of the incident ion beam. It is obvious that the motion of high-energy ions through the tracks exhibit a reduced electronic stopping power. The result is a deeper penetration of the ions trapped in tracks into the specimen, compared to the penetration of ions moving inside the undamaged matrix. The deep penetration of ions leads to a substantial increase in the width of the final distribution of the implanted atoms. If the tracks are practically hollow channels, similar to those observed by Vorob'eva et al. [136], we might expect the standard penetration depth R_p to double.

Here are the main features of this effect. First, the deeper penetration of impurities manifests itself with the fluences exceeding the threshold fluence. Second, the deeper penetration of ions shapes a specific 'tail' in the distribution of the implanted atoms. Usually, however, a delta-function Bragg distributions of implanted atoms with a sharp decline of the profile into the crystals is characteristic of high-energy ions. When the ion fluence becomes approximately 10^{12} – 10^{13} cm^{-2}, the entire irradiated surface is covered by tracks, and the probability of trapping subsequent incident ions in the tracks becomes significant.

Computer simulation of the penetration of high-energy ions into solids [137 – 141] revealed that among the effects characteristic of high-energy ion implantation, the fluctuations of the charge states and crystallographic channeling of ions have a pronounced influence on the profiles of the implanted atoms and the radiation-induced defects. Nevertheless, these factors alone cannot provide an explanation for the experimental data of Zaitsev et al. [123] and Burenkov et al. [140]. A more meaningful description of these data is achieved when channeling of ions along the tracks is accounted for.

Ion channeling along tracks is partially similar to ordinary axial crystallographic channeling. To describe the motion of swift ions in such tracks, we adapted (see Ref. [123]) the low-energy version of the Fokker – Planck equation developed by Beloshitskiĭ and Kumakhov (see Ref. [142]) for the channel-

ing of protons and alpha particles in crystals:

$$\frac{\mathrm{d}F(x, E_\perp)}{\mathrm{d}x} = \frac{\mathrm{d}}{\mathrm{d}E_\perp} \left[S(E_\perp)\, D(E_\perp)\, \frac{\mathrm{d}}{\mathrm{d}E_\perp}\, \frac{F(x, E_\perp)}{S(E_\perp)} \right]$$

$$- \frac{\mathrm{d}}{\mathrm{d}E_\perp} \left[\left(\frac{\mathrm{d}E_\perp}{\mathrm{d}x} \right)_{\mathrm{loss}} F(x, E_\perp) \right], \qquad (6.1)$$

where $F(x, E_\perp)$ is the distribution function of the channeled ions over the transverse energies $E_\perp$ at a depth x; $D(E_\perp)$ and $(\mathrm{d}E_\perp/\mathrm{d}x)_{\mathrm{loss}}$ are the diffusion coefficient and the drift velocity for the transverse energy, respectively, and $S(E_\perp)$ is the cross-sectional area of the channel accessible to ions with an energy $E_\perp$. The passage of ions dechanneled from the tracks is described by the Boltzmann transport equation [139].

The results of such a simulation are shown in Fig. 13. To be able to realistically describe the experimental results, one must allow for both the track channeling effect and the effect of fluctuations of charge states. On the final distribution, one can see a structure with two concentration peaks. The second peak is caused by track channeling. Numerical solution of equation (6.1) has shown that the effect of channeling along the tracks strongly depends on the track radius R_{tr}, the concentration N_d of defects (scattering centers) inside the tracks, and the channeling length L_{tr} inside a track. Only the experimental data on the distribution profiles of internal atoms and radiation-induced defects can be used to estimate the parameters R_{tr}, N_d, and L_{tr}. The following values of these parameters were used to arrive at the results presented in Fig. 13: $R_{\mathrm{tr}} = 0.6$ nm, $N_d = 0.002 N_a$, and $L_{\mathrm{tr}} = 3$ μm (N_a is the atomic number density). Note the good agreement between the results of calculations and the experimental data.

The profile of radiation damage measured for silicon irradiated by 377-MeV krypton ions [123] with a fluence of 4×10^{13} cm^{-2} revealed analogous peculiarities. The most vivid feature in the distribution of disturbances is the 'arm' at a depth of 50 μm, which extends 10 μm from the major peak in the distribution. A theoretical description of such an arm that allows for the channeling of ions in tracks has been carried
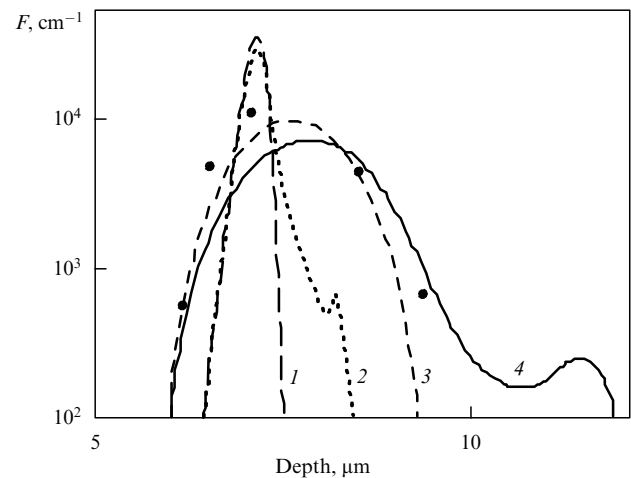
Figure 13. Depth distributions of implanted atoms in diamond irradiated by Xe$^+$ ions with $E = 130$ MeV: *1* — standard calculations, *2* — calculations that use the Boltzmann transport equation and allow for the motion of particles in the tracks, *3* — calculations that allow only for the effect of fluctuations of the charge states, *4* — calculations that allow for both effects, and • — the experimental data taken from Ref. [143]. All distributions are normalized to unity.

out by Zaitsev et al. [123] for the following values of the parameters: $R_{tr} = 0.9$ nm, $N_d = 0.02 N_a$, and $L_{tr} = 30$ μm.

Hence, one important result of the effect of channeling of ions along tracks on the distribution profiles of implanted impurities and radiation-induced defects is the deeper penetration of some of the ions into the specimen, which causes the appearance of a substantial concentration 'tail' (in some cases the tail has two peaks) directed into the depths of the crystal. The effect of fluctuations of the charge state of the ions manifests itself in the substantial broadening of the implantation profiles near the projected ion path. The mean range of ions, in the channeling-in-track mode, in diamond amounts to $1/2 R_p$. A theoretical estimate of the atomic number density near the track region yielded a value amounting to $0.5 - 2\%$ of the initial atomic number density in the matrix. The probability of light ions being dechanneled from the tracks proved to be $5 - 10$ times higher than that of heavy ions. Such a substantial distinction in the dechanneling effectiveness is, obviously, related to the difference in the structure of the latent track produced by light and heavy ions.

Recently, Bíró et al. [144] reported on the formation of carbon nanotubes when specimens of highly oriented pyrolytic graphite were irradiated by heavy ions with $E > 100$ MeV. The researchers observed individual carbon nanotubes several micrometers long by the methods of atomic-force microscopy and scanning tunnel microscopy inside and around the craters where dense nuclear cascades (the so-called Brinkman cascades) intersected the specimen surface and created vast areas of sputtering. Often, one or several nanotubes emerged from a sputtering crater. Hence, a simple way to produce carbon nanotubes is to employ the high-energy ion beam technique. Usually, carbon nanotubes are formed by an electric discharge, laser ablation, or catalytic decomposition of hydrocarbons [54]. In the first two technologies, the growth of carbon nanotubes takes place in a highly excited carbon plasma generated at high temperatures ($T \gg 1000 \,°C$).

7. Track formation in InP crystals

7.1 Track formation in InP crystals at room temperature

The most thorough and broad studies of track formation in semiconducting $III - V$ compounds have been done for the cases of irradiation of InP single crystals by high-energy xenon and krypton ions [109, 145 - 150]. Detailed TEM studies into the cross section of the crystalline InP irradiated by 250-MeV xenon ions with a fluence of 7×10^{12} cm^{-2} at room temperature revealed (see Fig. 14) the following main distinguishing features in the distribution of disturbances over the depth of the crystal [109, 146, 147]. Two basic zones of disturbances were found to form in InP as a result of irradiation by xenon ions. The first zone, formed at a depth between 19 and 21 μm, is a layer of highly disturbed InP consisting of amorphous and crystalline regions and coinciding, in position, with the peak in the elastically released energy. The second near-surface zone, down to a depth of 10 μm, contains latent tracks $7 - 15$ nm in diameter. The tracks are in the form of continuous straight cylinders several micrometers long (they are formed at depths ranging from 100 nm to 7 μm) or extended defects similar to chains of pearls, which are located along the ion paths at depths ranging from 35 to 100 nm and from 7 to 10 μm. But what is most interesting here is that the researchers recorded the
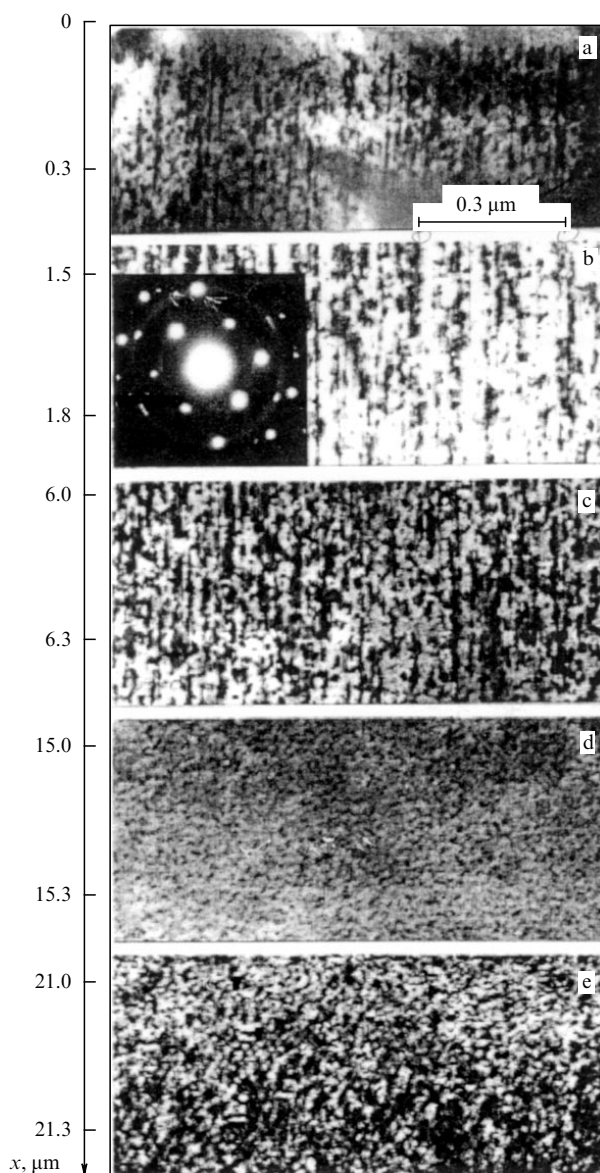

Figure 14. Bright-field XTEM (cross-sectional transmission electron microscopy) images for InP implanted with 250-MeV Xe$^+$ ions with a fluence of 7×10^{12} cm^{-2}, taken at different depths. Figure b also shows the appropriate diffraction pattern.

presence of practically defect-free surface layers approximately 35 nm thick and a maximum possible track density (about 2×10^{11} cm^{-2} at a depth of roughly 3 μm) that is much smaller than the ion fluence of 7×10^{12} cm^{-2}. In addition, they found that with a fluence of 250-MeV xenon ions lower than 5×10^{12} cm^{-2} no continuous tracks are formed — only small defects and clusters are detected. On the basis of the data of this research, a model of track formation in InP was proposed by Herre et al. [145] and Gaiduk et al. [147], which in turn was based on the thermal spike approximation and assumed that the material around the ion paths melts to depths at which the electron energy losses exceed the critical value $(dE/dx)_{e, thr}$ [151, 152]. The critical energy losses were found to depend on the material of the target (and on the degree of perfection of the crystal structure) and to reflect the effectiveness of the mechanism that transforms the energy of electronic excitations into

atomic motion, compared to the effectiveness of competing mechanisms responsible for the dissipation of the excitation energy. It was also demonstrated that the critical value of the electron energy losses in track formation in crystalline InP [145, 147] amounts to roughly 13 keV nm^{-1}.

Herre et al. [145] and Gaiduk et al. [147] suggested considering the specific features of solidification of the melt surrounding the ion paths as the second criterion of track formation. Track melting is accompanied by rapid cooling and resolidification of the surrounding matrix. In the parent specimen, the melted cores are surrounded by a perfect crystal, and in the course of hardening of the thermal spike epitaxial recrystallization must take place. However, the recrystallized region is not really perfect: it contains a certain number of point defects and defect complexes, as observed by Chew and Cullis [153] after the melting of GaAs by laser pulses. Epitaxial recrystallization of the track regions may not have been achieved by the time subsequent ions reach the crystal, since the surrounding crystal is already imperfect. Under subsequent irradiation, the recrystallization rate may become much smaller than the hardening rate, which results in 'freezing' of a sufficiently continuous amorphous track.

The model proposed by Herre et al. [145] and Gaiduk et al. [147] is capable of explaining the difference between the track density and the ion fluence, while the nearly defect-free thin near-surface layer can be interpreted as a layer produced by enhanced defect annealing which prevents defects from accumulating in the layer near the surface. Note that the accumulation of defects in the InP crystal in the course of its irradiation also stimulates the increase in the electron–phonon coupling constant or the decrease in the electron–phonon relaxation time in the thermal spike model. The latter factor drives the temperature in the track region up and leads to its melting even when $(dE/dx)_e < (dE/dx)_{e,\,thr}$. The effect of the previous injection of defects on track formation can be considered good proof that the model in question is valid.

In their experiment, Wesch et al. [148] produced a disturbed layer in a massive specimen of crystalline InP by pre-implanting in it 1-MeV Si$^+$ ions with a fluence of 2.5×10^{12} cm^{-2} at liquid-nitrogen temperature. Subsequent irradiation by 250-MeV xenon ions was carried out up to a fluence of 7×10^{11} cm^{-2}, i.e., roughly 10 times lower than the critical fluence for track formation in undisturbed InP. Electron-microscope studies revealed that tracks form at a depth of about 1 μm, which corresponds to the maximum in the elastically released energy for Si$^+$ ions with $E = 1$ MeV. At xenon ion fluences of 5×10^{13} cm^{-2} and higher two amorphous layers are formed: one at a depth region from the surface up to 10 μm, and the other at a depth of 19–21 μm, i.e., close to R_p.

7.2 Evolution of disturbances in crystalline InP irradiated by xenon ions at different temperatures

There is almost no discussion in the literature about the role that the temperature of irradiated crystals of semiconductors and insulators plays in track formation. Usually, the experiments are done at room temperature and rarely at liquid nitrogen temperature.

Figure 15 shows the results of TEM studies of InP crystals irradiated by 250-MeV xenon ions at different temperatures. The bright-field images of specimens prepared by the cross section method were taken at the same depth of approximately 3 μm. They clearly demonstrate that continuous tracks are formed under irradiation at room temperature
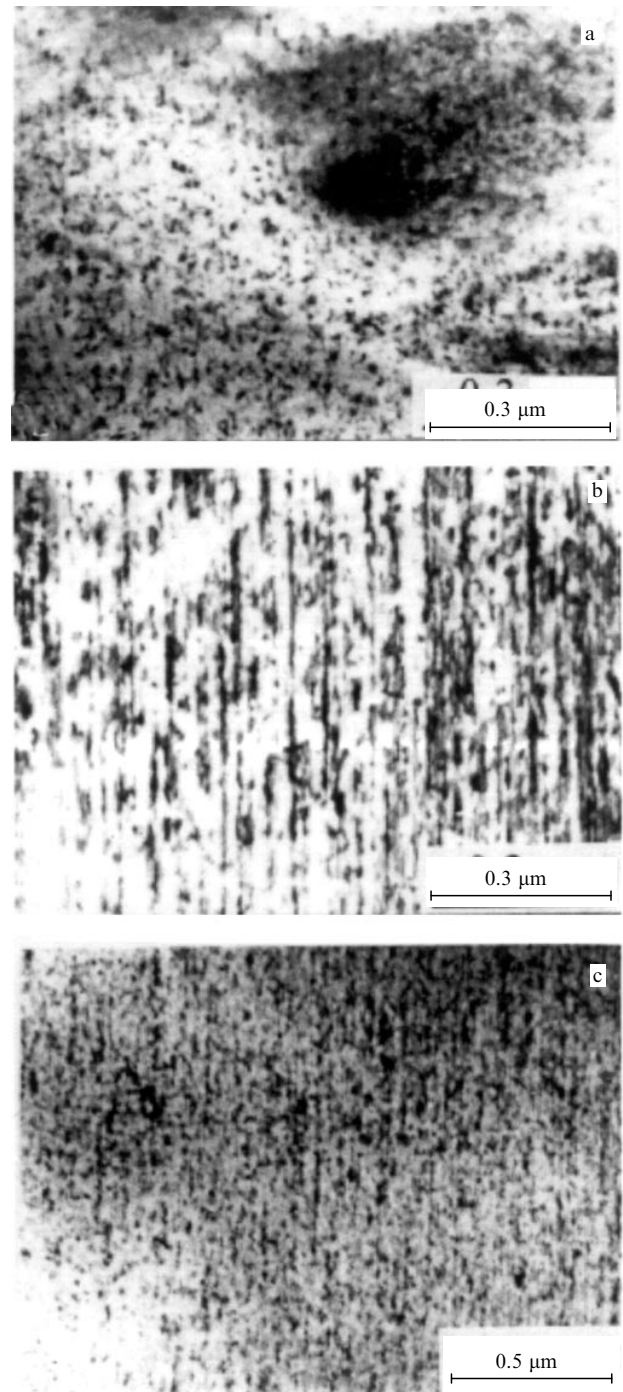
Figure 15. Bright-field images for InP implanted with 250-MeV Xe$^+$ ions at different temperatures: at room temperature (a), and at liquid-nitrogen temperature (b) with a fluence of 7×10^{12} cm^{-2}; at $T = 130\,^\circ$C with a fluence of 7×10^{14} cm^{-2} (c).

(Fig. 15a), and are absent in the case of irradiation at liquid-nitrogen temperature (Fig. 15b) and in the heated state (up to $T = 130\,^\circ$C) (Fig. 15c). After hot implantation, only separated, extended defects emerge; these defects are randomly arranged along the ion path and resemble a chain of pearls. Studies of disturbances with greater enhancement enable us to reveal an entirely different nature of defects in specimens irradiated at high and low temperatures. Interstitial dislocation loops with an average size of roughly 10 nm, small stacking faults, and microtwins with an average size in the
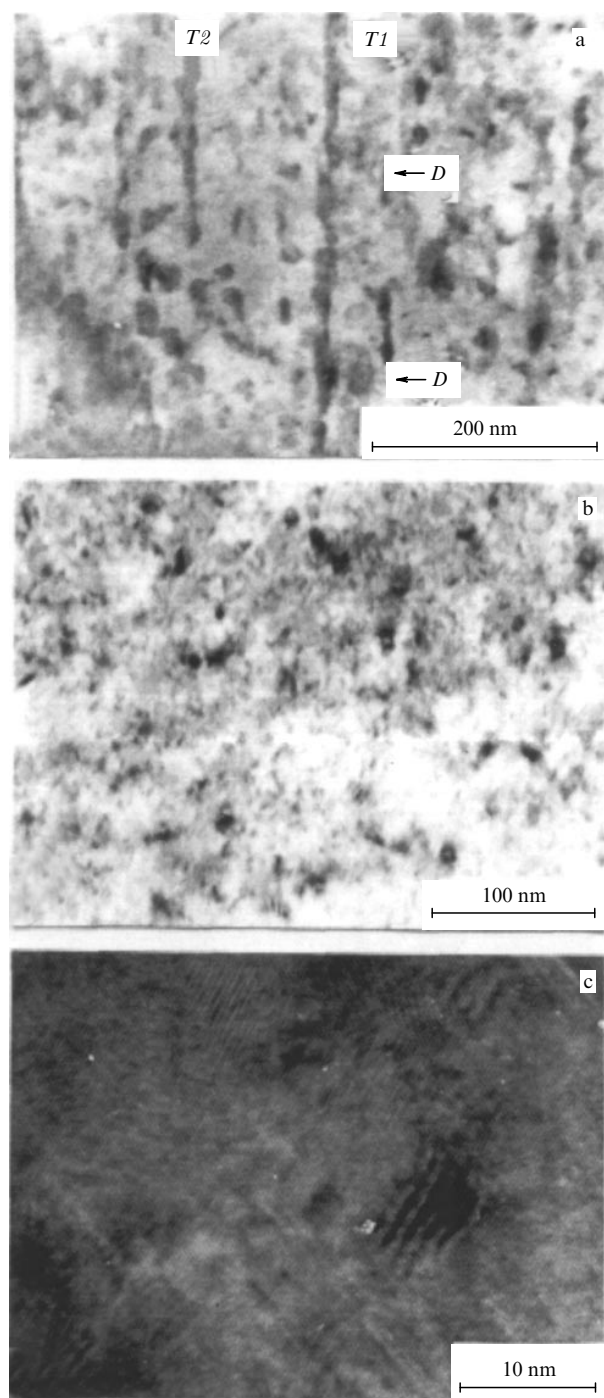
Figure 16. Enlarged bright-field images of the specimens similar to those in Figs 15a and 15c: (a) corresponds to Fig. 15a, and (b) corresponds to Fig. 15c. The image of the structure of the dark contrast region denoted by D in figure (a) was produced by high-resolution microscopy (c).

10 – 30-nm range are formed precisely in specimens irradiated at $T = 130\,^\circ\mathrm{C}$ (see Fig. 16b). Obviously, intense annealing of the initially generated defects (point defects, complexes of point defects, etc.) is accompanied by their transformation into more stable defects of the dislocation type *in situ* in the process of ion irradiation. Once again, these observations strongly support the basic idea of the model proposed by Herre et al. [145] and Gaiduk et al. [147], which implies that tracks form as a result of the solidification of a melted tube in a highly disturbed surrounding matrix. On the other hand, the

specimens that were irradiated at low temperature and at room temperature (T_{room}) were found to contain defects with amorphous cores. The reason why continuous tracks form at T_{room} but do not form at the liquid-nitrogen temperature $T_{\mathrm{l.n}}$ (80 K) is not clear so far, and the problem requires study in more detail. It can be inferred that this is because the heat conductivity of InP at $T_{\mathrm{l.n}}$ is approximately seven times higher than that at T_{room} [154], with the result that the melting of a track can be suppressed by intense dissipation of the electronic excitation energy in a large volume of the crystal. This assumption is currently being checked by applying the thermal spike model of Ref. [36].

7.3 Morphology of track regions
The enlarged bright-field TEM image of individual tracks for InP irradiated at T_{room} reveals its complex internal and external morphology (Fig. 16a). We see that the diameter of the track along its length varies in the 7 – 15-nm range (see the track labeled *T1*). It has been established that the thick segments of the track are usually accompanied by a more pronounced dark contrast in the surrounding matrix (labeled D on track *T1*). What is more, several thick segments of the track coincide with some other tracks or damaged regions localized nearby (e.g., see track *T2*). High-resolution investigations of the bright-field – dark-field contrast of the upper dark-contrast regions D (Fig. 16c) reveals patterns of the delta type and also moire patterns. Delta patterns point to the presence of the mosaic type structures with shifts and inclinations of individual blocks [155]. In a way similar to the external morphology, the image of an individual track is not uniform, which reflects its inhomogeneous internal structure. Microdiffraction measurements reveal that the track core is mainly amorphous, but still a small fraction of polycrystalline InP is also present [145, 147, 148].

The atomic structure of the tracks in different stages of track formation and their evolution can be analyzed on the basis of high-resolution transmission electron microscopy (HRTEM) images (see Fig. 17). Such analysis makes it possible to clarify several important characteristics of the atomic structure of tracks:

(1) most swift xenon ions generate defects around their paths, even in the absence of an amorphous core. This is clearly seen in Fig. 17a, where the region A has a weaker contrast compared to the periphery, with the assumption that A is the place where an ion hit the target. This ion did not create an amorphous core, but the lamellas of the microtwins (labeled T) nucleate at the center of the ion path and propagate over a distance of about 8 nm. Such defects — microtwins, stacking faults, and dislocation loops — can be seen near most of the tracks in Figs 17a – c. Unfortunately, point defects and defect complexes cannot be revealed by the given method. Nevertheless, the results of measurements done by the Rutherford backscattering spectroscopy (RBS) method in the ion channeling mode [145, 147, 148] indicate that there is accumulation of point defects;

(2) the first stage in the formation of an amorphous track can be seen in Fig. 17a, where small amorphous regions surrounded by microtwins and stacking faults are labeled B. The core of an amorphous track has an elliptic shape with approximately 5-nm major axis. The surrounding matrix has a crystal structure, but with a weak contrast, which may indicate the presence of point defects near the core. Another large (about 10 nm long) amorphous track that is almost circular is depicted in Fig. 17b. Nevertheless, apart from
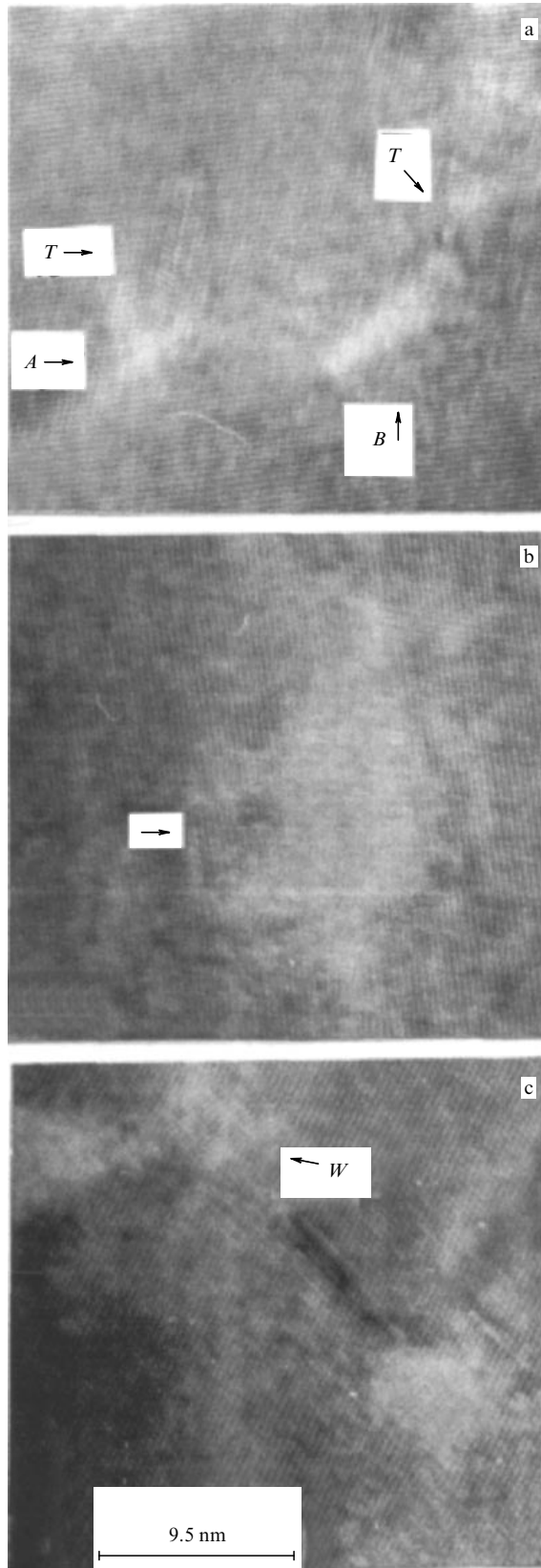
Figure 17. High-resolution images of the structure of InP implanted with 250-MeV Xe$^+$ ions at room temperature with a fluence of 7×10^{12} cm^{-2}, demonstrating a typical atomic structure of the tracks in different stages of track development (see the main text). Here, T represents microtwins and/or stacking faults, and W represents the wurtzite modification of InP.

amorphous material, a section of the track contains crystal particles indicated by an arrow, and finally

(3) Figure 17c illustrates an example of a phase transition in the track region. Microparticles of the wurtzite phase of InP have been discovered in several tracks (labeled W). These particles were identified by microdiffraction measurements and also from measurements of the interplanar distance for particles in images with atomic resolution [145–150]. As in the cases of silicon and germanium [156], the wurtzite modification of InP is expected to be a high-pressure phase [150]. The model of formation of the InP wurtzite modification in tracks and the transformation of this modification into a sphalerite phase under high irradiation fluences have been examined in Ref. [150].

The results of the studies considered here (see Refs [145–150]) can be explained by the thermal spike model if we additionally allow for the accumulation of disturbances due to the imperfect recrystallization of the melted tube surrounding the ion path. In other words, the presence of an incubation fluence for track formation, the effect of the previous injection of defects on track formation, and the discovered suppression of track formation under 'hot' and low-temperature irradiation corroborate this model. The slight contrast in the images with atomic resolution around the paths of some ions can be interpreted as caused by point defects (or complexes of point defects) that appear after imperfect recrystallization of melted tubes. Nevertheless, the formation of microparticles of the InP wurtzite phase, as well as the emergence of stacking faults and microtwins around the paths of the ions that had passed through the target can hardly be interpreted only as the result of solidification of the melt. Such structural defects and phase transitions can be created at high pressures, i.e., in shock waves generated by swiftly moving heavy ions.

7.4 Fluctuation mechanism of discontinuous-track formation in solids by swift ions

Many experimentalists (e.g., see Refs [114, 145, 157, 158]) who studied track formation in materials subjected to irradiation by high-energy ions recorded discrete, or discontinuous, tracks whose geometry varied from quasi-continuous to bead-like as the ions moved deeper into the target. Various mechanisms were proposed in order to explain these data (see Refs [126, 157, 159]). Tombrello et al. [159] assumed that tracks are formed mainly because of ionization of the inner shells of atoms in the stopping medium, and this process is accompanied by intensive production of low-energy delta electrons. According to the researchers, the discreteness of the tracks is a consequence of the discreteness peculiar to the ionization of inner electron shells. Nevertheless, Tombrello et al. [159] noted that only a small fraction of the ion energy can be released as a result of the ionization of inner shells of the atoms in the stopping medium and assumed that the main 'fuel' for track formation is the continuous addition of the ion energy to the electron subsystem of the solid. Moreover, they assumed that on those sections of the ion paths in the target where there is no ionization of inner electron shells the tracks are not formed. Ertchak et al. [126] attribute the discreteness of the track structure to the discreteness of formation of an electron flux along the ion path, which is brought about by momentum conservation.

It is believed that the most productive suggestion was put forward by Dartyge and Sigmund [157], who assumed that

the mean number of defects observed in a track is directly related to fluctuations in the ionization density rather than to the mean value of this quantity. However, as in the other approaches discussed earlier, here the researchers do not take into account the primary processes related to statistical fluctuations of the charge state of the ions moving in the solid, fluctuations caused by the atomic stripping and trapping of electrons. In our opinion it is precisely the fluctuations of the ion charge state that can lead to a substantial change in the losses of energy imparted to the electron subsystem on certain sections of the ion paths. These processes become significant when the energy of a moving ion is close to that corresponding to the threshold value of the mean energy losses $(dE/dx)_{e,thr}$ for track formation.

Thus, the discontinuous tracks observed in experiments can be caused by statistical fluctuations in charge exchange processes with the ion losing one or several electrons, when, over a certain section of the ion path, $(dE/dx)_e$ becomes larger than $(dE/dx)_{e,thr}$ for track formation. The mean ion range before the ion changes its charge state will determine the length of the defective region in the continuous track and the distance between such defects, while the diameter or geometry of the defect is determined by the number of stripped electrons in a single act. The idea has been discussed earlier in Refs [53, 141, 160, 161].

As noted earlier, the model that is used most often to describe the process of track formation is the thermal spike model. Although it agrees well qualitatively with the experimental data, there is still the question of why the latent heat of melting is not taken into consideration by this model. Also unresolved is the problem of the role of phonons in the energy spread from the excited region and the very idea of phonons is unclear when the temperature is 2000 K or higher. Apparently, the plasma approximation is more meaningful here [162, 163].

One must be especially careful when studying the processes of energy transfer from the excited region around ion paths in the case of metals and narrow-gap semiconductors. Indeed, the typical time of cooling of the electron plasma through electron heat conduction in metals does not exceed 10^{-14} s even at plasma temperatures of order ε_F, when the electron thermal diffusivity is at its minimum [163]. Thus, the plasma cooling time is shorter than the typical thermal oscillation time ($\sim 10^{-13}$ s), i.e., during cooling of the electron plasma the electrons interact with almost all immobile individual atoms (ions) rather than with collective atomic (ionic) oscillations.

A modified thermal spike model in which the region around an ion track is considered a two-component plasma consisting of electrons and highly ionized target atoms has been proposed in Ref. [164]. Such an approximation is meaningful since in the initial stage of penetration an ion ionizes the target atoms closest to its path to a very high degree. Using the irradiation of InP by swift xenon atoms as an example, this model was able, with additional allowance for fluctuations of the charge state of ions (see Section 7.4.1 below), to explain the main distinguishing features of track formation observed in InP crystals and discussed in Sections 7.1 – 7.3.

7.4.1 Stopping and charge exchange. When high-energy ions are injected into the target, elastic energy losses play a secondary role, and more than 90% of the ion energy is lost in inelastic collisions (i.e., in collisions with the target
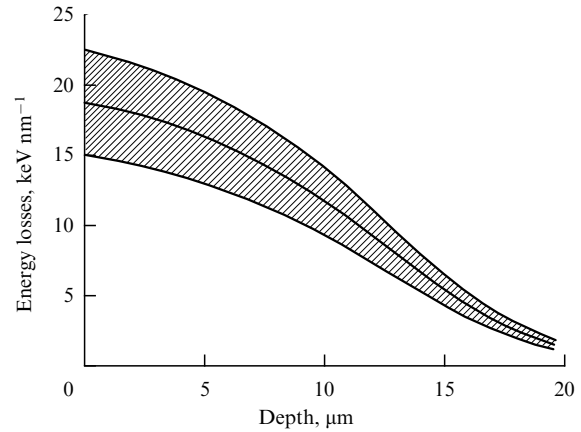

Figure 18. Energy losses vs. depth for 250-MeV xenon ions. The hatched area corresponds to the possible fluctuations of the dynamic ion charge.

electrons). This stopping process is described by the Bethe formula [165]

$$\left(\frac{dE}{dx}\right)_e = \frac{4\pi Z_2 Z_{1,eff}^2 e^4 N_a}{m_e v^2} \ln\left(\frac{2m_e v^2}{I}\right), \qquad (7.1)$$

where $Z_{1,eff}$ is the effective ion charge, Z_2 and N_a are the charge and number density of the target atoms, respectively, v is the ion velocity, m_e and e are the electron mass and charge, and I is the average ionization potential for the atoms of the crystal. Numerical integration of equation (7.1) yields a dependence of $(dE/dx)_e$ on depth x, represented in Fig. 18, for 250-MeV Xe^+ ions (the middle curve in the figure).

According to Herre et al. [145], who experimentally studied the track formation in InP irradiated by 250-MeV Xe^+ ions, the high ion energy losses are characteristic of the region where continuous tracks form [at depths $x \leqslant 7$ μm it appears that $(dE/dx)_e \geqslant 14$ keV nm^{-1}], while low energy losses are typical of the region without tracks [at depths $x \geqslant 10$ μm it appears that $(dE/dx)_e \leqslant 10$ keV nm^{-1}]. Discontinuous tracks were observed in the intermediate region 7 μm $\leqslant x \leqslant 10$ μm [145].

One of the processes that could lead to the above phenomenon is the fluctuation of the charge state of the moving ions, which is accompanied by a decrease or increase in the ion charge by one or several units (the processes of electron trapping or atomic stripping, respectively). To simplify the statistical picture of variations of the ion charge distributions over the target's depth, characteristic of a large ensemble of moving particles, let us examine the role of such fluctuations with respect to the mean effective ion charge $Z_{1,eff}$. Allowing for the fact that track-formation phenomena and the real pattern of a track recorded by the HRTEM method are related to an actual individual ion, one can think of this approach as justified. The statistical nature of the ion distribution over charge at any depth for the entire particle flux manifests itself in the spread of the characteristics (the length of the continuous and discontinuous sections of a track, the diameter of each such section, etc.) of individual tracks in relation to the mean characteristics.

It is a well-known fact (e.g., see Refs [165–167]) that a swift ion moving inside a solid loses some of its electrons, so that its charge may change from zero to the atomic number Z_1. Due to the processes of electron loss and trapping, this

charge does not remain constant: it fluctuates about its mean value. Only in the case of well-channeled ions may the charge state of the ions prove to be 'frozen' [166, 168–170] because of the low electron density in the central part of the channel along which the ions move. For instance, high-energy channeled oxygen ions ($E = 35$ MeV) with an initial charge $q_{ent} = 8$ passed through single-crystal silicon films ($\langle 110 \rangle$-channels) that were 340 nm thick almost without changing their sign [168], which is an indication that the cross sections of electron trapping by such ions are very low ($\leqslant 2 \times 10^{-19}$ cm^2). Such cross sections are approximately a hundred times smaller than the trapping cross section (1.8×10^{-17} cm^2) for 35-MeV O^{+8} ions in argon [166]. The cross sections of trapping and losing electrons by channeled 40-MeV O^{+7} and O^{+8} ions in $\langle 110 \rangle$-channels of silver and gold amount to about 10^{-19} cm^2, so that the charge of the particles remained 'frozen' as the ions passed through a crystal that was approximately 1 μm thick. Thus, oriented crystals are able to 'strip' swift ions more effectively than amorphous or polycrystalline targets. According to the calculations done in Ref. [166], the equilibrium charge distribution of 40-MeV oxygen ions in silver (without channeled particles) has to set in after the ions traverse a distance of approximately 40 nm in the crystal.

Several formulas have been proposed in order to describe the processes of ion charge exchange (e.g., see the formulas given in Refs [166, 167]). A beam of ions that have traveled through a sufficiently thick solid acquires an equilibrium charge distribution resembling the Gaussian distribution

$$F_q \approx (2\pi d^2)^{-1} \exp\left[-\frac{(q - q_0)^2}{2d^2} \right] \tag{7.2}$$

with two parameters: the average charge $q_0 = \sum_q q F_q$, and the distribution's half-width d, where $d = [\sum_q (q - q_0)^2 F_q]^{1/2}$, with q being the ion charge.

Within a broad range of ion velocities, where $q \approx (0.3 - 0.8) Z_1$, the value of d is practically independent of v. In the general case, d is approximately described by an expression derived by Dmitriev and Nikolaev [171]:

$$d = d_1 \left\{ q_0 \left[1 - \left(\frac{q_0}{Z_1} \right)^k \right] \right\}^{1/2}, \tag{7.3}$$

where d_1 and k are the empirical parameters, with $d_1 = 0.5$ and $k = 0.6$.

The frequently observed asymmetry in the distribution (7.2) as well as the large width of the distributions are mainly caused by the processes of multielectron losses in a single collision.

In the case at hand, the average effective ion charge $Z_{1,\,eff}$ can be found by using the semiempirical expression from Ref. [171], while the fluctuations of this charge can be calculated from the Bohr formula [165]:

$$q_0 = Z_1 \left[1 + \left(\frac{1}{Z_1^\alpha} \frac{v}{v'} \right)^{-1/k} \right]^{-k},$$

$$\sigma_0 \approx \pi a_0^2 (Z_1^{1/3} + Z_2^{1/3}) \left(\frac{v_0}{v} \right)^2, \tag{7.4}$$

where for the sake of making estimates it is assumed that $Z_{1,\,eff} \approx q_0$ (a more rigorous expression relating these two quantities can be found in Ref. [139]), σ_0 is the electron

capture/loss cross section, v is the ion velocity, α and v' are the empirical parameters, a_0 is the Bohr radius, v_0 is the electron velocity in the first Bohr orbit of the hydrogen atom, $k = 0.6$, $v' = 3.6 \times 10^6$ m s^{-1}, $v_0 = 2.19 \times 10^6$ m s^{-1}, $\alpha = 0.48$, and $a_0 \approx 0.053$ nm. For xenon ions with $E_0 = 250$ MeV in InP in the region of a discrete track, this yields $q_0 \approx 25$ and $\sigma_0 \approx 1.8 \times 10^{-17}$ cm^2.

Note that the study of the distributions of the injected ions over their ranges with allowance for the fluctuations of charge states, done in Ref. [141], shows that only at fairly large depths do the charge distributions come to an equilibrium. For instance, in silicon, $z \approx 0.8$ μm for 50-MeV B$^+$ ions, and in diamond, $z = 1$ μm for 59-MeV Ni$^+$ ions. As Z_2 increases, the depth z decreases. Thus, for 250-MeV Xe$^+$ ions in InP, the average charge differs substantially from $Z_{1,\,eff}(E)$ in the initial segment of the ion path after the ions have entered the crystal, with the result that the ion energy losses per unit path, $(dE/dx)_e$, are substantially lower than the value predicted by Bethe's formula (7.1). These estimates help to elucidate the observations made in Ref. [145], namely, the absence of tracks and the exhibition of weak disturbances in the near-surface area of the crystal at depths $x \leqslant 35$ nm, and the presence of discontinuous tracks at depths beginning at 35 nm down to roughly 100 nm. Continuous tracks are observed only at depths $x \geqslant 100$ nm down to $x \approx 7$ μm. Discontinuous tracks appear again at depths $7 \leqslant x \leqslant 10$ μm, where $(dE/dx)_e$ become nearly equal to or smaller than $(dE/dx)_{e,\,thr}$. The thickness of each of the regions increases with an the ion energy almost in direct proportion [150], i.e., for Xe$^+$ ions with an energy of 340 and 250 MeV the ratio of the thicknesses for the corresponding regions is approximately 1.36 (340/250).

According to equation (7.1), even a small variation in the effective charge may lead to sizable fluctuations in the ion energy losses. For instance, the loss (trapping) of only one electron results in oscillations in $(dE/dx)_e$ of about 8%, i.e., $(q_{max}/q_{min})^2 \approx 1.08$, while the loss (trapping) of three electrons gives rise to oscillations amounting to 30%. The hatched area in Fig. 18 indicates the possible energy losses if the loss (trapping) of up to two electrons is taken into account. These estimates, in addition to the available experimental data, suggest the following model.

At small depths measured from the target surface, where the ion flux distribution over the charges has yet to reach equilibrium, the energy losses may be lower than the threshold value for track formation, with the result that only simple point defects and complexes of such defects form at such depths. The surface, being an effective sink for such defects, will substantially suppress their final concentration. As the ions move deeper into the target, multielectron charge-exchange processes lead to fluctuations in the mean charge, when the energy losses are higher than the threshold value for track formation, i.e., $(dE/dx)_e > (dE/dx)_{e,\,thr}$. The mean free path of an ion in a higher charge state determines the length of the defective section of a discontinuous track. It must be stressed once more that some concepts of the statistical theory of ion penetration through solids are true for the case of an individual ('statistic mean') ion. On a continuous track, $(dE/dx)_e$ is much larger than $(dE/dx)_{e,\,thr}$. When the energy losses become comparable to the threshold losses for track formation (e.g., the melting of the local region and so forth), oscillations in the stopping caused by ion charge-exchange processes lead to repeated crossing of this threshold and, hence, to formation of a discontinuous track. At larger depths

such crossings rarely occur and the time they take is very short, i.e., rare and short defective regions are formed. One should note here the important role of rare, close elastic collisions of ions and the atoms of the medium, collisions that stimulate charge-exchange processes accompanied by the loss of several electrons. At still larger depths the elastic collisions of ions with the atoms of the medium begin to play the main role; such collisions result in the formation of ordinary structural defects and amorphous regions.

This model has been substantiated by calculations of the average defect size in discontinuous tracks. As noted earlier in the given section, the length of such sections is equal to the mean free path of the ion before the next charge-exchange event takes place. The probability p of this process occurring at a distance x can be calculated by the formula $p = N_a \sigma_0 x$, where N_a is the atomic density in the target. Then, the length of a defect in a discontinuous track is defined as $\lambda = 1/N_a \sigma_0$. The magnitude of the latter quantity, which takes into account only one-electron charge-exchange processes, is 2 – 3 times smaller than the size of the observed defects [145, 150]. According to the results mentioned in Betz's review [167], the relative probability for multielectron charge-exchange processes with swift ions compared to one-electron charge-exchange processes is about 60% for the loss or trapping of two electrons, 40% for three-electron processes, 20% for four-electron processes, and so forth. Multielectron processes lead to large fluctuations in the energy losses [see formula (7.1)]. When two- and three-electron losses are taken into consideration, the calculated length of defects becomes approximately 2 – 3 times larger than when only one-electron processes are accounted for, which both qualitatively and quantitatively corresponds to the experimental data, taken from Refs [114, 145, 150], on the lengths of the detected defect regions.

It should be emphasized that the theory developed in Refs [137 – 139, 141] for determining the correct ion distribution over ranges with allowance for fluctuations of the ion charge distributions has made it possible to substantially improve the correspondence of the theoretical profiles for the implanted atom distribution over the depth in the target to the experimental data. The magnitudes of the distribution widths obtained in this theory are 1.5 – 5 times greater than those calculated by traditional methods without allowance for the fluctuations indicated [172]. However, in all cases the theoretical profiles proved to be narrower than those examined in experiments. Only one-electron charge-exchange processes are taken into account in the theory developed in Refs [137 – 139, 141]. Apparently, the role of multielectron charge-exchange processes is also important in such complicated problems as the distribution of high-energy ions over ranges in solids. As noted earlier in this section, allowing for multielectron processes has a marked effect on the width of charge distributions for an ion flux.

8. Track formation in inorganic insulators

The processes of track formation in insulators, caused by electronic stopping of swift ions, differ very significantly both in the characteristics of the track regions and in the possible mechanisms of formation of such regions. More than one hundred original papers and more than a dozen of reviews devoted to this topic have been published (e.g., see Refs [50, 65, 158, 173 – 183]). Silk and Barnes [184] were the first to observe latent tracks in an electron microscope (1959), and

Price and Walker [185] applied chemical etching and optical microscopy, to detect tracks produced by fission fragments in mica. Later on, the morphology of the track was studied by various methods, which revealed spherical discontinuous and cylindrical continuous regions of structural disturbances.

Analysis of the experimental data on track formation makes it possible to single out several important factors that must be taken into account when using the various models of track formation:

(a) the electronic properties of the irradiated material play an important role (metal, semiconductor, or insulator, the presence of a Fermi surface, the size of the band gap, and the electron – phonon relaxation time);

(b) the structural state of the target (single crystal, amorphous material, polycrystalline material; grain size, and the presence and type of structural defects, boundaries, and impurities) determines the electron – phonon relaxation time, the temperature near a track path, and the possibility and rate of epitaxial recrystallization;

(c) the composition and structural complexity (type of a unit cell) of the irradiated material determines the effectiveness of the epitaxial recrystallization of the local region;

(d) the possibility of two-component crystals becoming amorphous depends on the strength of the constituent ionic bond. The effectiveness of track core formation and the core size for amorphized materials are much greater than for nonamorphized materials. For instance, the radius of the track core in quartz α-SiO$_2$ [186] is much larger than in LiF [187], and finally

(e) the initial spatial distribution of the energy imparted into the electron subsystem and the energy spectrum of electronic excitations determine the temperature of the local region near an ion path during thermalization of the excited region. Thus, for equal values of $(dE/dx)_e$, the ion with the higher velocity generates a larger radial distribution of the released electron energy in the stopping medium (because of an increase in the number and velocity of delta electrons), which causes the track to have a smaller radius [188].

What is important in track formation is the presence of a threshold and the size of this threshold, $(dE/dx)_{e, thr}$. Table 3 illustrates the threshold stopping powers for a number of inorganic materials. As in semiconductors, the tracks can be continuous or discontinuous. Continuous tracks have been detected in a number of insulators, including SiO$_2$ and LiNbO$_3$ [188], for 1 – 5-keV nm^{-1} range of energy losses by heavy ions. The track regions in these materials are in the amorphous state. Heavy ions moving with velocities corresponding to energy losses of approximately 10 keV nm^{-1}

Table 3. Threshold energy losses $(dE/dx)_{e, thr}$ for track formation in different materials.

Material	$(dE/dx)_{e, thr}$, keV nm^{-1}	References
SiO$_2$	2	[189]
Mica	5	[189]
LiNbO$_3$	7	[189]
Y$_3$Fe$_5$O$_{12}$	4	[189]
LiF	10	[190]
Al$_2$O$_3$	21	[189]
MgO	20	[189]
Bi	31	[189]
Fe	40	[2]
YBaCu$_3$O$_7$	30	[180]

produce tracks in LiF detected by chemical etching and the small-angle X-ray scattering (SAXRS) method [190]. The morphology of the tracks in this case proves to be more complex and is characterized by the presence of a small defective core and a large-radius peripheral region with a dispersive distribution of defects. Nevertheless, in some insulators, such as MgO and Al_2O_3, the threshold values of $(dE/dx)_e$ are much larger than the above-mentioned values and amount to about 20 keV nm^{-1}. Discontinuous tracks have been detected at the threshold value of energy losses [191, 192]. Even higher specific ion energy losses are needed for tracks to form in semimetals, monatomic semiconductors, high-T_c superconductors, and metals (Table 3).

8.1 Possible mechanisms of track formation in insulators

The possible mechanisms of track formation in insulators are under discussion. Fleischer et al. [50] have related track formation to the breakdown of the insulator due to the strong electric field that is induced in the space between the electrons injected from the region near a track path and the positive ions remaining in this region. In a similar interpretation this process is also called a Coulomb explosion or Coulomb repulsion [193]. However, a quantitative model based on this mechanism has yet to be developed.

An approach based on the rupture of atomic bonds in solids, caused by intense electronic excitations, has been proposed by Tombrello et al. [194–197]. The transport of energy from the region closest to an ion path is carried out by energetic secondary electrons whose maximum velocity is proportional to the ion velocity. The secondary-electron energy density e^* has been numerically simulated by Waligorski et al. [38] and can be approximated by the following expression:

$$e^*(r) = \frac{\gamma}{2\pi R_\perp^\gamma} \left(\frac{dE}{dx} \right)_e \frac{1}{r^{2-\gamma}}, \qquad (8.1)$$

where $R_\perp$ is the maximum radial range of the secondary electrons ($R_\perp = 840\varepsilon/\rho E$, where ρ is the density of the material in units of g cm^{-3}, and ε is the ion energy in units of MeV a.m.u.$^{-1}$), and γ is an adjustable parameter: $0 < \gamma < 1$.

Assuming that for a given target material the atomic bonds in the target are ruptured when the released energy density e^* is higher than a certain value e_c^*, we can rearrange equation (8.1) to another form that enables the calculation of the track radius R_c as a function of the same quantities as in Eqn (8.1):

$$R_c = \left(\frac{\gamma}{2\pi e_c^*} \frac{dE}{dx} \right)^{1/(2-\gamma)} \frac{1}{R_\perp^{\gamma/(2-\gamma)}}. \qquad (8.2)$$

If a discontinuous track with k defective regions per unit length is formed, the methods that measure the volume of the damaged material determine only the mean volume A_{eff} of the space occupied by the track,

$$A_{eff} = \pi R_c^2 \lambda k, \quad R_{eff} = R_c \sqrt{\lambda k}, \qquad (8.3)$$

where λ is the length of each damaged region, and R_{eff} is the average radius of the discontinuous track. For spherical regions, $\lambda = 4R_c/3$.

In calculating the continuous tracks in $Y_3Fe_5O_{12}$, very good agreement with the experimental data on R_c was observed at $\gamma = 0.27$ and $e_c^* = 0.024$ eV $Å^{-3}$ for practically

all values of ε and various ions including C_{60} and C_{20} clusters [195]. The same parameters make it possible to describe (with a 25% accuracy) the experimentally detected track diameters for such materials as quartz and white mica [195]. For the high-temperature superconductor YBCuO, Tombrello [196] found that $e_c^* = 0.047$ eV $Å^{-3}$, i.e., track formation in conducting materials requires a much higher density of the energy imparted into the electron subsystem. In the case of track formation in organic materials, the above values of e_c^* and γ usually guarantee reasonable agreement between R_c and the available experimental data (see Ref. [195]). However, an empirical adjustment of e_c^* is needed it we want all the experimental data to agree, with an accuracy of at least 10%, with the values calculated by formula (8.2). Thus, for a polystyrene target, the optimal value of e_c^* is 0.014 eV $Å^{-3}$ for all ions and energies; for Mylar (a polyester film), this value varies from 0.007 eV $Å^{-3}$ for light penetrating ions to 0.016 eV $Å^{-3}$ for implanted uranium ions, and for cellulose triacetate, which is sensitive to track formation even in the case of proton irradiation, the value of interest is $e_c^* = 0.0009$ eV $Å^{-3}$.

The most common approach in interpreting the experimental data on track formation in insulators is to apply the thermal spike model (see Refs [198–200, 183] and the works cited therein, and also Section 3). Lifshits et al. [28] described the physical and mathematical features of this model, and later the model was actively developed by Toulemonde and his group [37, 183, 201, 202] in order to describe track formation in insulators. The basic thermal parameters of the model, such as the specific heat capacity C_e and the heat conductivity K_e of the electron subsystem, are unknown for insulators. Baranov et al. [61] assumed that the hot electrons in the conduction band of insulators are similar to the hot electrons in metals and arrived at following expressions: $C_e = (3/2)N_e k_B$, where N_e is the number of electrons participating in the diffusive propagation of energy, and $K_e \approx 2$ J cm^{-1} K^{-1}. The electron–phonon coupling constant g is also unknown for insulators. It is related to the electron–phonon interaction time τ_a through the formula $\tau_a = C_e/g$, and to the mean free path λ for electron–phonon interaction through the formula $\lambda^2 = D_e\tau_a = D_e C_e/g = K_e/g$, where D_e is the thermal diffusion coefficient. In all computations λ was considered an adjustable parameter. For instance, in calculations of the track radius in quartz, λ was assumed to be equal to 4 nm [183], with the result that $\tau_a = 8 \times 10^{-14}$ s.

Materials that can exist in the amorphous state, such as SiO_2 (band gap $E_g = 12$ eV), $Y_3Al_5O_{12}$ ($E_g = 6.3$ eV), $Gd_3Ga_5O_{12}$ ($E_g = 4.8$ eV), $LiNbO_3$ ($E_g = 4.8$ eV), GeS ($E_g = 1.7$ eV), $BaFe_{12}O_{19}$ ($E_g = 1$ eV), and $YBa_2Cu_3O_{6.9}$ ($E_g \approx 0$), exhibited an interesting λ vs. E_g empirical dependence (Fig. 19), which apparently correctly reflects the real dependence of g, and hence of λ, on E_g. When $E_g > 2.8$ eV, there was only a slight drop in λ (from 5 to 4 nm), which suggests that the characteristics responsible for energy transfer from the electrons to the atoms of a target are roughly the same for all insulators.

For insulators that cannot exist in the amorphous state (i.e., they are crystals) and in which the ionic bond prevails, such as LiF ($E_g = 14$ eV), SnO_2 ($E_g = 3.6$ eV), and GaF_2 ($E_g = 11.5$ eV), the λ vs. E_g dependence is similar (see Fig. 19). To describe the track radii, Toulemonde et al. [183] assumed that in amorphized materials there forms a quasi-melted phase, while in those that cannot be in the amorphous state, the energy per atom imparted into the atomic subsystem by
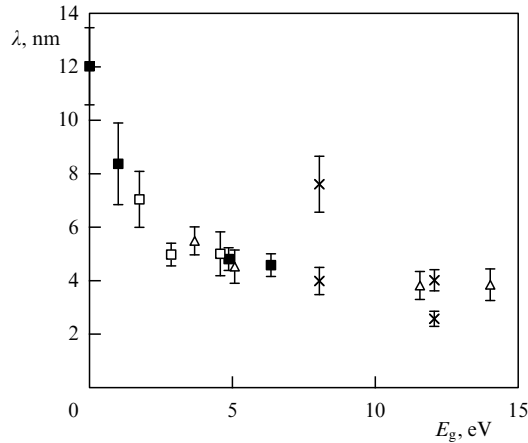
Figure 19. The mean free path λ for the electron-lattice coupling as a function of the band gap E_g [183]. Here ■ stands for the data for amorphisized materials, □ for amorphisized materials with allowance for latent heat of melting, △ for nonamorphisized materials, and × for Al_2O_3 and SiO_2.

excited electrons reaches the energy of sublimation if the atoms are near the surface or the binding energy for atoms in the bulk of the material.

It is difficult to classify sapphire Al_2O_3 with $E_g = 8$ eV as a material that can or cannot be in the amorphous state [203]. If the experimental data are interpreted on the basis of the two approaches (discussed above) to track formation, we get different values for λ: 8 nm if we assume that there is a melted phase, and 4 nm on the basis of the criterion that the energy imparted by the excited electrons into the atomic subsystem must be higher than the binding energy of the atoms (see Fig. 19). Earlier, a similar dependence of λ on E_g was discussed by Katin et al. [204].

Szenes [205–207] used the thermal spike mechanism to construct a convenient model for calculating the track radii in amorphisized materials. The model describes the effect of ion velocity on the size of tracks.

One must note, however, the morphological difference of tracks (see Section 8.2) in amorphisized and nonamorphisized materials and also the earlier-mentioned ambiguity in interpreting the results on track formation in nonamorphisized materials in the thermal spike model. For such materials, and especially alkali-halide crystals, the excitonic model is, probably, the most suitable one. A qualitative picture of this model was given by Itoh and Stoneham [189], while the quantitative aspects were discussed by Yavlinskii [208].

Itoh and Stoneham [189] assumed that the difference in the threshold values of $(dE/dx)_{e,\,thr}$ for track formation in insulators can be explained by the magnitude of the exciton-phonon cohesion force. The self-trapping (autolocalization) of a dense excitonic cluster (with a local density close to molecular density [209], i.e., almost one exciton for each molecular unit) causes amorphization or produces severe structural disturbances. Approximately within 10 fs after an ion has hit the target, its energy is transferred to the creation of energetic holes in the valence band and electrons in the conduction band; such holes and electrons have relatively moderate energies and are unable to initiate further ionization of atoms. Since the ranges of the primary delta electrons are really not long, almost all released energy is concentrated at a short distance from the ion path. Thus, in the region

surrounding an ion path a dense medium of electron-hole pairs is generated, with the process accompanied by heating. The generation of a high-density electron-hole medium immediately produces excitons that form an excitonic cluster [189].

An excitonic cluster evolves along one of three paths: Auger recombination, diffusion away from the ion path, and lattice deformation (disturbance or heat release) due to autolocalization of excitons. The first process leads to heating; the second is responsible for energy transfer away from the ion path, and the third, which occurs only in materials in which excitons form clusters (autolocalization), transforms the energy of electron-hole pairs into lattice deformation, which in turn may result in the formation of structural disturbances. The relaxation of an excitonic cluster is, in a way, similar to the hot zone in a cascade of collisions: each lattice atom in such a zone is drastically displaced.

Exciton autolocalization occurs in materials for which $(dE/dx)_{e,\,thr}$ exceeds roughly 5 keV nm^{-1} [189]. And since the formation of autolocalized excitons brings about substantial changes in the volume of the material, the Itoh and Stoneham model [189] can explain the experimentally examined swelling of the material that accompanies track formation [190]. In material in which excitons do not autolocalize, the threshold energy losses for track formation increase by a factor of four to eight (see Table 3). The absence of autolocalization causes a diffusion outflow of no less than 1/3 of the released energy from the region surrounding the ion track [189].

Yavlinskii [208] assumed that, in contrast to metals, in insulators the excited electrons can move only together with holes, which ensures quasi-neutrality. Such a dense electron-hole plasma begins to expand because of internal pressure. The process resembles an explosion. The swelling stops after $\tau \approx 10^{-13}$ s, when electron-phonon coupling comes into the picture and also autolocalized states appear (a gas of autolocalized excitons with a number density $n \leqslant 10^{21}$ cm^{-3}). The radius of the exciton cloud is $R(\tau) \approx \sqrt{3}C_0\tau \approx 10^{-5}$ cm, and the profile of the exciton number density is described by the following expression [29]

$$n(r, t) = \frac{N_0}{\pi R^2(t)} \exp\left(-\frac{r^2}{R^2(t)}\right), \qquad (8.4)$$

where $N_0 = \pi r_0^2 N_a$ is the initial number density of electron-hole pairs per unit length, with N_a the atomic density, and $r_0 = R(0)$ the initial radius of the excited region, $R(t)$ is the radius of swelling of the cylindrical excited region, and $C_0 \approx \sqrt{T_0/m_e}$ is the initial thermal velocity, with T_0 the initial electron temperature. The final expressions for the radius of the excited region and the temperature of the electron-hole pairs in such an approximation assume the form [208]

$$R(t) = \sqrt{\frac{3}{\pi^{1/2} r_0 m_e}} \left[\frac{1}{(3\alpha/2 + \beta)N_a}\left(\frac{dE}{dx}\right)_e\right]^{1/4} t, \qquad (8.5)$$

$$T_e(t) = \frac{r_0 m_e^{2/3}}{3^{2/3}\pi^{1/6}} \left[\frac{1}{(3\alpha/2 + \beta)N_a}\left(\frac{dE}{dx}\right)_e\right]^{1/6} \frac{1}{t^{4/3}}, \qquad (8.6)$$

where α and β are the parameters used in calculations and determined by the ionization equilibrium and the ionization potentials of the atoms [210].

The energy released in the annihilation of autolocalized excitons is the direct cause of defect formation. According to equation (8.6), the temperature of the exciton gas at the end of the swelling process is about 100 K, i.e., there is no substantial heating of the lattice in such an insulator.

8.2 Defect formation and track formation in alkali-halide crystals

Radiation-induced disturbances made by electron and X-ray irradiation of alkali-halide crystals have been studied for many decades [211–213]. It has been established that primary Frenkel defects, F- and H-centers, are formed thanks to radiationless decay of autolocalized excitons [214]. An F-center is an electron on an anion vacancy. At room temperature, the most important types of defects in LiF are F-centers and F_n-centers (aggregates of F-centers with $n = 2, 3 \ldots$), which are identified by an absorption band in the UV region of the spectrum. V_k-centers are holes localized in the lattice. H-centers are stable in LiF only at $T \leqslant 60$ K. In addition, in alkali-halide crystals there are also charged Frenkel defects, i.e., empty halogen vacancies and interstitial halogen ions, called α- and I-centers (they emerge as a result of tunnel recombination of primary Frenkel defects, i.e., F- and H-centers). Under prolonged irradiation, the concentration of such centers may become very high. For instance, when KBr crystals are irradiated at $T = 10$ K, the ratio of the number of generated Frenkel α-and I-pairs to the number of F- and H-centers is approximately equal to $4-5$.

Ion irradiation of LiF colors the crystal (color centers appear in the crystal) in a color gamma ranging from yellow to dark brown, depending on the fluence. Various methods are used in studies of disturbances and tracks in alkali-halide crystals. Among these are optical absorption, SAXRS, chemical etching, scanning atomic-force microscopy (SAFM), and surface profilometry.

Track formation in alkali-halide crystals has most thoroughly been studied in LiF [183, 190, 215–217]. Within a large cylindrical halo (several dozen nanometers in diameter) surrounding a path of swift ions there are point defects, such as F- and F_2-centers exposed by the optical absorption method, and similar disturbances characteristic of ordinary types of irradiation (electrons and X-rays). If $(dE/dx)_e$ of the ions amounts to approximately 10 keV nm^{-1}, more complex defects form within a very small core of the track region with a radius of $1-2$ nm. This central part is exposed by SAXRS and chemical etching. The track core consists of quasi-cylindrical discontinuous regions of complex defects (supposedly small colloids of Li atoms, molecular complexes of fluorine, and vacancy clusters). Trautmann et al. [190, 217] used the optical absorption method and discovered substantial swelling caused by ion irradiation. This swelling can be assigned to a track radius of $5-10$ nm, i.e., is characteristic of the intermediate zone between the track core and the halo. It manifests itself at much lower threshold energy losses of about 4 keV nm^{-1}.

There are also other important features of track formation in LiF. The color center concentration increases with ion fluence, and for an ion fluence at which individual track regions overlap the concentration of F-centers becomes saturated. The F-center concentration takes a value of approximately 10^{19} cm^{-3}, which is typical to the beginning of agglomeration of simple defects into defect clusters under high irradiation fluences of electrons or gamma quanta.
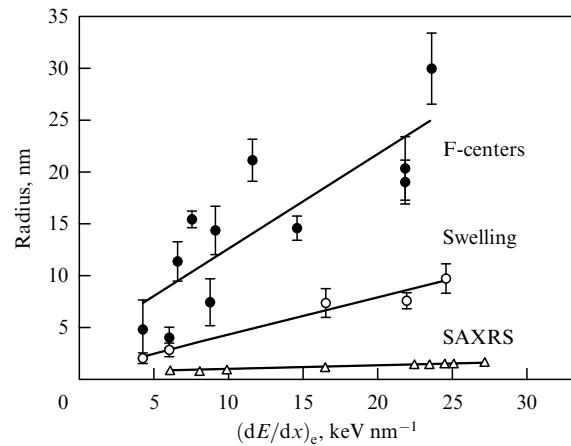

Figure 20. Track radii in LiF, obtained by the methods of optical absorption spectroscopy (F-centers), profilometry (swelling), and small-angle X-ray scattering (SAXRS) [190].

While color centers are annealed even at $T \leqslant 300$ °C, the effectiveness of chemical etching and the SAXRS contrast remain almost the same up to 400 °C, as well as at irradiation temperatures as low as 15 K [218].

Such behavior of the results of chemical etching and of the SAXRS contrast at low temperatures is, to a certain extent, unexpected and points to the nonthermal nature of the agglomeration of defects in the track core, since usually at low temperatures the generation of F-centers is strongly suppressed.

The track radius determined by F-centers is approximately 5 nm for irradiation by light ions, e.g., sulfur ions (4.3 keV nm^{-1}), and increases to 30 nm for irradiation by Au ions (24 keV nm^{-1}) (Fig. 20). The radius values obtained from SAXRS measurements are approximately 10 times smaller than those obtained in optical absorption spectroscopy measurements (see Fig. 20). The values of $(dE/dx)_{e, thr}$ appropriate for identifying track regions by the SAXRS method and chemical etching are close and amount to about 10 keV nm^{-1}. There is also a dependence of the track core size on the ion velocity at equal values of $(dE/dx)_e$ [190].

The swelling in nonamorphisized alkali-halide crystals (LiF and CaF_2) under irradiation by swift heavy ions helps in establishing a general tendency (the dependence on fluence, $(dE/dx)_e$, and R_p) characteristic of amorphisized materials, such as Al_2O_3, $LiNbO_3$, $Gd_3Ga_5O_{12}$, and quartz α-SiO_2 [190]. What proved unexpected is that for a given type of ion with a given energy, the swelling in LiF is approximately the same as in an amorphisized material, in which this phenomenon is caused by a substantial variation of density in the phase transition from the crystal state to the amorphous state. In amorphisized materials whose radii of amorphous track regions have been determined by the high-resolution transmission electron microscopy (HRTEM) method, the radius values differ by only $10-20\%$ from those determined from the data on swelling. Both effects in these materials correspond to the same value of the threshold ion energy loss.

Jensen et al. [219] applied the HRTEM method to observe the tracks generated by the irradiation of CaF_2 crystals by cluster ions Au^+ (20.2 MeV), C_5^+ (20.2 MeV), C_{10}^+ (20.2 MeV), and C_{60}^+ (30.2 MeV). The track diameters amounted to 4.9, 2.95, 6.1, and 10.9 nm, respectively. According to the researchers, the tracks consist of aligned anion pairs or

calcium inclusions. Irradiation of the luminescent crystals CsI and CsI-Tl by Kr^+ ions with $E = 8.63$ MeV a.m.u.$^{-1}$ at $T = 15$ K [214] was found to lead to formation of a pronounced absorption band related to F-centers. In addition to this band there was a broad absorption band located between the exciton and F-center bands. This additional band was associated by the researchers with the presence of anion vacancies, an α-center, autolocalized holes, V_k-centers and interstitials, and H-centers [214].

Lightly ($\approx 10^{17}$ cm^{-3}) thallium-doped CaF_2 crystals exhibits a lower radiation resistance to the generation of F-centers than pure CaF_2. At the same time, heavily doped CsI-Tl gave no indications of F-center formation.

Pariselle et al. [220] irradiated the mixed alkali-halide crystals $K_{0.8}Rb_{0.2}I$ by 13.6-MeV argon ions in the $20-200$-K temperature range. They found that at 20 K F-center formation was completely suppressed, while at 100 K it was negligible. The total rate of defect generation at 20 K is higher than at 100 K. Ion bombardment at 20 K causes the formation of such defects as H- and I-centers (these defects are known to have a low thermal stability). This is an indication that for these materials the thermal spike effects do not manifest themselves and have no influence on the formation and stabilization of structural defects.

8.3 Processes accompanying the passage of swift ions through oxide materials

A lot of research into defect formation and track formation in such oxide materials as $Y_3Fe_5O_{12}$, $BaFe_{12}O_{19}$, $SrFe_{12}O_{19}$, AFe_2O_4 (A = Mg, Ni, or Zn), $Bi_2Fe_4O_9$, $YBa_2Cu_3O_{7-\delta}$, $LiNbO_3$, Al_2O_3, UO_2, and SiO_2 was done in the 1980s and 90s (see the review [182] and the references cited therein). Most often, the following methods were utilized in such research: SAXRS, high-resolution electron microscopy, and Rutherford backscattering spectroscopy (RBS) in the ion channeling mode. In the surface approximation we can find the fraction d of the damaged material directly from the RBS spectra (in the ion channeling mode). Assuming that there has been no annealing, we can use the model of direct disordering in defect formation for predicting the following kinetics of the process: $d = 1 - \exp(-A^*Dt)$, where D is the ion fluence, and A^* is the cross-sectional area of the disturbed region produced by the passing ion. In the case of cylindrical tracks, the effective radius R_{eff} of the cylinder can be calculated by the formula $A^* = \pi R_{eff}^2$.

8.3.1 Morphology of tracks and threshold energy losses for track formation in oxide materials.
Systematic studies of defects produced by swift heavy ions in magnetic insulators have been carried out by Houpert et al. [221], Studer and Toulemonde [179], Costantini et al. [222, 223, 225], and Meftah et al. [224]. On the basis of the results of their studies we can indicate five specific regions (Fig. 21) characterizing the morphology of the tracks. The large spread in track radii for the same value of $(dE/dx)_e$ testifies to the important role of ion velocity. As noted earlier, for equal values of $(dE/dx)_e$ the lower ion energy corresponds to the higher density of the released energy and, respectively, the larger radius of the latent track. In most cases the tracks in magnetic insulators are amorphous regions. Their size and formation features can be described fairly well by the thermal spike model [182, 226]. The passage from the amorphous phase of the track to the crystal matrix is extremely abrupt both in the case of magnetic insulators and in such materials as $YBa_2Cu_3O_{7-\delta}$, $ZrSiO_4$ and

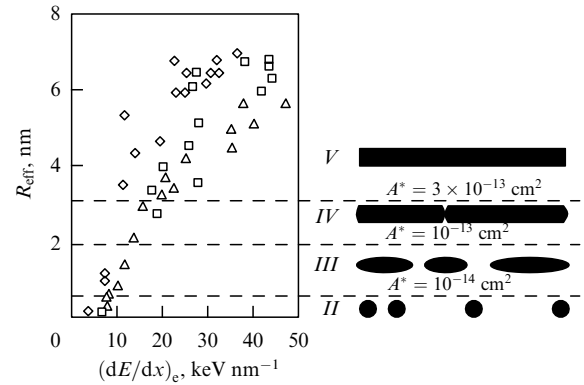**Figure 21.** Effective radius as a function of $(dE/dx)_e$ and the corresponding morphology of track regions in $Y_3Fe_5O_{12}$ [221], with $R_{eff} = (A^*/\pi)^{1/2}$. Open lozenges represent the values for ion energies in the $0.03-2$-MeV a.m.u.$^{-1}$ range, open squares represent values for ion energies in the $2-8$-MeV a.m.u.$^{-1}$ range, and open triangles represent values for ion energies in the $8-30$-MeV a.m.u.$^{-1}$ range. The region I, in which damage (amorphous regions) is produced by nuclear collisions ($A^* \approx 10^{-18}-10^{-16}$ cm^{-2}), is not shown.

so forth [182]. This permits the determination of the track sizes with reasonable rigor.

Houpert et al. [221] studied the evolution of track region morphology with the variation of $(dE/dx)_e$ for such materials as $Y_3Fe_5O_{12}$, $BaFe_{12}O_{19}$, $NiFe_2O_4$, and $MgFe_2O_4$ at ion energies ranging from 8 to 40 MeV a.m.u.$^{-1}$. Here are some characteristic features of these observations. TEM images show continuous and discontinuous cylindrical regions and spherical defects along the ion path (see Fig. 21). The region II in Fig. 21, where $R_{eff} < 0.56$ nm and $A^* < 10^{-14}$ cm^2, corresponds to the case where electron disturbances prevail over nuclear ones. Extended defects are almost perfect spheres with a diameter of 3 nm. The region III, where $0.56 < R_{eff} < 1.8$ nm and $10^{-14} < A^* < 10^{-13}$ cm^2, corresponds to the case where spherical defects overlap and cylindrical defects with a diameter of 3 nm form. For $1.8 < R_{eff} < 3.1$ nm and $10^{-13} < A^* < 3 \times 10^{-13}$ cm^2, the cylindrical defects begin to overlap and chemical etching of latent tracks becomes effective (region IV). For $R_{eff} > 1.3$ nm and $A^* > 3 \times 10^{-13}$ cm^2, the defective regions are long continuous cylinders of amorphous material and the presence of a homogeneous disturbance inside the cylinder becomes evident. In the case of $Y_3Fe_5O_{12}$ irradiated by ions with an energy of about 12 MeV a.m.u.$^{-1}$ in the high-rate mode [224], the energy losses in the range $4.5 < (dE/dx)_e < 7$ keV nm^{-1} correspond to formation of spherical defects with $R_{eff} > 1.3$ nm.

For $7 < (dE/dx)_e < 14$ keV nm^{-1}, the spherical defects percolate and discontinuous cylindrical defects with $R_{eff} = 1.5$ nm form. But for $14 < (dE/dx)_e < 20$ keV nm^{-1}, there is percolation of cylindrical defects, and the track radius begins to grow. Continuous long cylindrical tracks form for $(dE/dx)_e > 20$ keV nm^{-1}. A similar picture was observed by Dartyge et al. [227] and Albrecht et al. [228] in the irradiation of mica. In mica irradiated by an ion beam directed along the normal to the cleavage plane, the track regions are cylinders containing amorphous material [229–233]. The boundary separating the amorphous region from the crystal matrix is abrupt, i.e., there is no intermediate region and no contrast of stresses, so characteristic of GeS crystals [231].

The threshold energy losses at which extended defects emerge in other magnetic insulators, such as $BaFe_2O_{10}$ and $NiFe_2O_4$, amount to 10 and 14 keV nm^{-1}, respectively [179]. Continuous amorphous tracks in $ZnFe_2O_4$ have been observed under ion irradiation with $(dE/dx)_e = 26$ keV nm^{-1}, but have not been detected at $(dE/dx)_e = 16$ keV nm^{-1} [158]. The dependence of track morphology on the amount of energy imparted into the electron subsystem of high-temperature superconductors is illustrated in Table 4. Continuous column-like tracks (containing amorphous material) with a diameter of 7 nm have been produced in the high-T_c ceramic material $YBa_2Cu_3O_7$ by 6-GeV Pb$^+$ ions with $(dE/dx)_e = 40$ keV nm^{-1} [234]. Irradiation by 6-GeV uranium ions with $(dE/dx)_e = 50$ keV nm^{-1} produces amorphous tracks with a diameter of about 11 nm in the thallium high-T_c ceramic material $TlBa_2Ca_2Cu_3O_8$ [234]. Cylindrical track regions in high-T_c materials bring about a drastic increase in the critical currents at high temperatures and in strong magnetic fields. This useful effect can be explained as the consequence of effective pinning of magnetic lines of force by cylindrical (column-like) structural defects [234–238].

Table 4. Dependence of track morphology on $(dE/dx)_e$ in high-T_c ceramic materials [180, 234–236].

Ion	E, GeV	$(dE/dx)_e$, keV nm^{-1}	Morphology
		$YBaCu_3O_7$	
Br	1.4	11	No
Xe	3.5	19	Discontinuous
Sn	0.58	28	Discontinuous
Pb	5.3	35	Continuous
Au	1.0	38	Continuous
		$Bi_2Sr_2Ca_1Cu_2O_8$	
I	0.5	27	Continuous
		$Tl_2Ba_2Ca_2Cu_3O_8$	
Pb	6	40	Continuous

Two different approaches to the problem of correct interpretation of the amorphous track regions detected in quartz SiO_2 have been developed by French researchers [239, 240]: Toulemonde et al. [239] constructed the thermal spike model, which has become the standard model in this area of research, while Douillard and Duraud [240] invoked the mechanism of point defect peak. The formation of continuous amorphous tracks in $LiNbO_3$ is characteristic of ion energy losses $(dE/dx)_e > 10$ keV nm^{-1}, while the formation of discontinuous tracks consisting of isolated defects is intrinsic to ion energy losses $(dE/dx)_e < 10$ keV nm^{-1} [241, 242]. Continuous tracks prove to be surrounded by a stressed-crystal shell. Such crystals exhibit enhanced track diffusion of additionally implanted europium atoms [242].

The formation of amorphous tracks is also a characteristic feature of such materials as $KTiOPO_4$ [243], UO_2 with threshold losses $(dE/dx)_{e, thr} \geqslant 22 - 29$ keV nm^{-1} [244, 245], MoO_3 and MoS_2 [114], TeO_2 (with, according to the literature, the biggest track radius) [226], and RCO_2, where $R =$ Y, Tm, and Ce (ferromagnetic amorphous tracks in a paramagnetic matrix) [246]. Vorob'eva et al. [136] discovered hollow channels along ion paths in gypsum irradiated by xenon ions with $E = 1$ MeV a.m.u.$^{-1}$. The researchers explained this feature by the remarkable structural properties of gypsum crystals. Other experiments exposed a substantial reduction of the atomic number density in the track core region. For instance, in zircon [128], the atomic number density inside the track made by ions of Pb with $E = 14$ MeV a.m.u.$^{-1}$ amounted to only 10% of the atomic matrix density. In polymers, this value amounted to 12% [240], and the track density in $YBa_2Cu_3O_7$ after irradiation by 1-GeV ions of Au amounted to 20% of the initial density of the material [180]. The formation of through holes with a diameter of approximately 5 nm has been detected in films of the nanosized powder of SnO_2 irradiated by ions of Pb with $E = 4.6$ MeV a.m.u.$^{-1}$ [247]. Similar results were obtained in the case where such films were irradiated by ions of Ta, Pb, and U with $(dE/dx)_e \geqslant 40$ keV nm^{-1} [248]. This effect was explained by Berthelot et al. [248] in terms of the thermal spike model as the result of evaporation of the material inside the track.

The results achieved by Rodichev et al. [249], who fabricated silicon nonocrystallites ($2 - 3$ nm in diameter) in SiO_2 in the tracks formed as a result of irradiation of α-SiO by ions of Ni and Pb, are interesting from the standpoint of applications. This method makes it possible to create quantum dots and wires and to control the optical properties of materials.

A number of researchers have also studied the tendency toward track formation in wide-gap insulators resisting attack by radiolysis. The irradiation of Al_2O_3 by swift ions with $(dE/dx)_e = 24 - 44$ keV nm^{-1} generates a large number of disturbances, and the effective track diameter varies from approximately 3.6 to 5.2 nm as the specific energy losses increase [191, 250]. One question has remained unanswered, however: Was the track core amorphous or disordered but in the crystal state? For Al_2O_3 and MgO, Thevenard et al. [251] found that the threshold energy losses $(dE/dx)_{e, thr}$ for defect formation are 20 and 22 keV nm^{-1}, respectively, but that the track core becomes amorphous only when this value exceeds 40 keV nm^{-1}. Skuratov et al. [252] observed a sharp drop in the ratio of the luminescence intensities for F- and F$^+$-centers in the polycrystalline corundum Al_2O_3 irradiated by swift ions with $(dE/dx)_e \geqslant 5$ keV nm^{-1}. An almost continuous amorphous layer 2 μm thick is formed in the corundum irradiated by 85-MeV iodine ions with $(dE/dx)_e \geqslant 4 - 5$ keV nm^{-1} and a fluence of 2.8×10^{14} cm^{-2} [253]. The thickness of this layer increases to 4.5 μm as the fluence increases to 1.2×10^{15} cm^{-2}. These results suggest that the structural state of the material has a strong influence on the threshold energy losses for defect and track formation. On the whole, both sapphire and corundum are highly stable against amorphization caused by elastic collisions. For instance, several dozen displacements per atom are needed for corundum to become amorphous at $T = 200$ K [253]. It should be stressed that, on the whole, amorphization by electronic excitations is more effective than by nuclear collisions [182]. The released energy density for amorphization in the electronic stopping mode is at least five times lower than in the nuclear stopping mode [254].

$MgAl_2O_4$ crystals, which have the same band gap as Al_2O_3 (9 eV), possess even higher stability against amorphization caused by elastic collisions [255]. One of the possible reasons for so high a radiation resistance of $MgAl_2O_4$ compared to that of corundum Al_2O_3 is the much lower value of the energy of migration of interstitial atoms (0.21 eV compared to 0.6 eV) [256]. Irradiation of polycrystalline

$MgAl_2O_4$ targets by 430-MeV Kr^+ ions and by 614-MeV Xe^+ ions triggers the formation of almost continuous tracks with diameters of roughly 2.0 and 2.6 nm, respectively [256]. According to Zinkle and Skuratov [256], the irradiation by swift heavy ions causes structural disorder to set in octahedral cations but does not create an amorphous core in the tracks, as noted earlier for Al_2O_3 and MgO. Nevertheless, it must be noted that recrystallization of an amorphous spinel may easily occur through ionization in $100-200$-keV electron irradiation [256] in TEM studies. Formation of a continuous amorphous layer on this spinel takes place during irradiation by 72-MeV iodine ions with greater fluences (10^{16} cm^{-2}) and with $(dE/dx)_e \geqslant 8$ keV nm^{-1} at $T = 300$ K [256]. However, the precise mechanism by which such an amorphous layer is formed has yet to be established: it is either direct amorphization in separate tracks or amorphization caused by multiple overlapping of disturbed crystalline ion tracks.

In oxide materials, the size of the track radius depends essentially on the resistance of the material under similar conditions of ion irradiation (Table 5). Hence, the electronic properties of the irradiated materials must be taken into consideration when building a rigorous theory of track formation.

Table 5. Comparison of the sensitivities of different materials for $(dE/dx)_e = 25$ keV nm^{-1} and an ion energy of 2 MeV a.m.u.$^{-1}$ [182]; R_{tr} is the measured track radius.

Material	R_{tr}, nm	Energy density, eV per atom	Resistivity, Ω cm
SiO_2	7	1.2	$10^{14}-10^{16}$
$Y_3Fe_5O_{12}$	4.5	2.2	10^{12}
$BaFe_{12}O_{19}$	4.0	2.2	10^5
$MgFe_2O_4$	3.4	1.7	5×10^{-3}
$ZnFe_2O_4$	2.0	2.0	5×10^{-2}
$YBa_2Cu_3O_{7-\delta}$	1.5	3.0	5×10^{-3}

9. Conclusions

Analysis of the processes accompanying the penetration of superhigh-energy ions through solids suggests that intense electronic excitations play an important role in generating structural defects, in the intense inelastic sputtering of materials, and in the initiation of a number of specific effects, such as track formation, local melting, amorphization, and the production of high-pressure phases, fullerenes, and carbon nanotubes.

The possible mechanisms of track formation are still being discussed. However, the large volume of contemporary experimental data suggests that in most insulators, semiconductors, and dispersed materials with metallic conduction the processes of formation of melted regions followed by their rapid solidification are the reason for the structural and phase changes recorded in the irradiated materials. The thermal spike model makes it possible to correctly interpret most experimental data for such materials. For such materials as alkali-halide crystals, the most suitable model today is the excitonic model [189, 208].

Depending on the type of metal and its structural state, the transfer of a large amount of energy into the electron subsystem may lead both to the annealing of earlier produced and genetic structural defects and to high effectiveness of defect formation, which is greater than the effectiveness of nuclear stopping processes by a factor of 20

or more. Some metals exhibit track-like formation of defect condensates which accumulate in the cylindrical region along the ion path.

Amorphous alloys and compounds with metallic conduction subjected to the same conditions of ion irradiation reveal the presence of strong radiation-induced creep accompanied by a sizable variation of the transverse dimensions and the thickness of the objects.

The manifestation of track formation, the phase composition of the tracks, and the track morphology depend on a number of important factors, namely,
- the electronic properties of the irradiated material (metal, semiconductor or insulator, band gap, and electron–phonon relaxation time);
- the structural state of the target (single crystal, amorphous material, polycrystalline material, grain size; the presence and type of structural defects, boundaries, and impurities), which determines the electron–phonon relaxation time, the temperature near the ion path, and the possibility and rate of epitaxial recrystallization;
- the compositional and structural complexity of the irradiated material, which also determines the rate of epitaxial recrystallization of local regions;
- the possibility of two-component crystals becoming amorphous, which depends on the strength of the constituent ionic bond, and
- the initial spatial distribution of the energy imparted into the electron subsystem and the energy spectrum of the electronic excitations, which determine the temperature of a local region in the stage in which the excited region is thermalized. For instance, for equal values of $(dE/dx)_e$, the ion with the greater velocity generates a larger radial distribution of the energy imparted to the electrons of the stopping medium, which results in the smaller track radius. The excitations with the highest density correspond to the case in which materials are irradiated by cluster ions (e.g., fullerene ions).

The process of forming latent tracks accompanied by brief chemical etching is widely employed in practice to manufacture filters (based on polymer materials with pores whose dimensions are in micrometer, submicrometer, and nanometer ranges) for the chemical, medical, and biological industries, and to fabricate metal nanowires in polymers, magnetic multilayer nanowires, and highly sensitive sensors [257].

However, the specific structure of the track regions makes it possible to predict that in the 21st century they will be widely used in other industries and areas of human endeavor.

As shown in the present review, the hollow or almost hollow track regions can be filled with atoms of almost all kinds due to the process of track migration of atoms from the surface layer or from the matrix. Here, the diffusivity of the atoms along the track channels is many orders of magnitude larger than its value for undisturbed material. Bearing in mind that the diameter of each track is often varied from 1 to 10 nm, we can estimate the number of tracks within one square centimeter of the surface at 10^{12}. Thus, the packing density of elements in such a system of nanoelectronics may be as high as 10^{12} elements to each square centimeter (or even higher), i.e., the density is 10^3 higher than the value that can be achieved today. The possibility of electron tunneling through the walls of neighboring isolating channels makes it possible to predict the creation of new classes of nanoelectronic devices. The unique optical, photoelectric, and conducting

properties of tracks may lead to a new generation of electronic and optoelectronic nanosized devices.

The processes of formation of continuous and discontinuous tracks in materials with supersaturated solid solutions are of interest if we want to fabricate ordered systems of quantum wires and chains of quantum dots. Here, ordinary ion implantation can be used to achieve supersaturation in impurities.

Being effective materials for track formation, plastics are widely used at present in radiobiological dosimetry as detectors of the radioactive gas radon, which is a health hazard [258]. Such detectors are especially effective in monitoring the concentration of radon in living quarters by gathering data with the track technique. The material of the detectors is then chemically etched and the tracks are detected by conventional optical means. Measuring the emanation of radon from the ground over large areas by the track method makes it possible to predict severe earthquakes [258].

Track technology is the future means of increasing critical currents and magnetic field strengths in high-T_c ceramic materials, of forming quantum dots and quantum wires in insulators by precipitating one of the components of the material, of intensifying adhesion of metallic layers to polymers, and of fabricating ferromagnetic nanosized wires in paramagnetic materials.

References

1. Dunlop A et al. *C.R. Acad. Sci. Ser. II* **309** 1277 (1989)
2. Dunlop A et al. *Nucl. Instrum. Meth. B* **48** 419 (1990)
3. Audouard A et al. *Europhys. Lett.* **3** 327 (1991)
4. Dunlop A et al. *J. Phys.: Condens. Matter* **2** 1733 (1990)
5. Audouard A et al. *Nucl. Instrum. Meth. B* **59/60** 414 (1991)
6. Audouard A et al. *Radiat. Eff. Defects Solids* **110** 113 (1989)
7. Balanzat E *Radiat. Eff. Defects Solids* **126** 97 (1993)
8. Rivière J P et al. *Nucl. Instrum. Meth. B* **59/60** 781 (1991)
9. Tombrello T A *Nucl. Instrum. Meth. B* **95** 501 (1995)
10. Dufour Ch et al. *Nucl. Instrum. Meth. B* **107** 218 (1996)
11. Dammak H, Dunlop A, Lesueur D *Nucl. Instrum. Meth. B* **107** 204 (1996)
12. Dunlop A, Dammak H, Lesueur D *Nucl. Instrum. Meth. B* **112** 23 (1996)
13. Wang Z G et al. *Nucl. Instrum. Meth. B* **107** 175 (1996)
14. Dufour Ch, Paumier E, Toulemonde M *Nucl. Instrum. Meth. B* **122** 445 (1997)
15. Ossi P M, Pastorelli R *Nucl. Instrum. Meth. B* **122** 566 (1997)
16. Barbu A et al. *Nucl. Instrum. Meth. B* **145** 354 (1998)
17. Slowinski B *Nukleonika* **44** (2) 271 (1999)
18. Henry J et al. *Nucl. Instrum. Meth. B* **67** 390 (1992)
19. Dunlop A et al. *Europhys. Lett.* **15** 765 (1991)
20. Legrand P et al. *Mater. Sci. Forum* **97 – 99** 587 (1992)
21. Dunlop A, Lesueur D *Mater. Sci. Forum* **97 – 99** 553 (1992)
22. Dammak H et al. *Phys. Rev. Lett.* **74** 1135 (1995)
23. Dunlop A et al. *Nucl. Instrum. Meth. B* **36** 412 (1989)
24. Dammak H et al. *Radiat. Eff. Defects Solids* **126** 111 (1993)
25. Barbu A et al. *Europhys. Lett.* **15** 37 (1991)
26. Trautmann C et al. *Radiat. Eff. Defects Solids* **126** 207 (1993)
27. Dunlop A, Lesueur D *Radiat. Eff. Defects Solids* **126** 123 (1993)
28. Lifshits I M, Kaganov M I, Tanatarov L V *At. Energ.* **6** 391 (1959)
29. Davydov A A, Kalinichenko A I *Probl. Yad. Fiz. Kosm. Luchei* **26** 60 (1986)
30. Martynenko Yu V, Yavlinskiĭ Yu N *Dokl. Akad. Nauk SSSR* **270** 88 (1983) [*Sov. Phys. Dokl.* **28** 391 (1983)]
31. Glushtsov A I et al. *Dokl. Akad. Nauk Belorussk. SSR* **31** 609 (1987)
32. Averback R S, De La Rubia T D, Benedek R *Nucl. Instrum. Meth. B* **33** 693 (1988)
33. Koponen I *Nucl. Instrum. Meth. B* **71** 234 (1992)
34. Yoffa E J *Phys. Rev. B* **21** 2415 (1980)
35. Toulemonde M et al. *Nucl. Instrum. Meth. B* **112** 26 (1996)
36. Kamarou A A, Malafei D A, Shchehlik V S, in *Proc. of the II Intern. Conf. CFDM-98 "Finite-Difference Methods: Theory and Applications"* Vol. 2 (Minsk, 1998) p. 56
37. Wang Z G et al. *J. Phys.: Condens. Matter* **6** 6733 (1994); Erratum, ibid. **7** 2575 (1995)
38. Waligorski M P R, Hamm R N, Katz R *Nucl. Tracks Rad. Meas.* **11** 309 (1986)
39. Komarov F F, Novikov A P, Hoang A T *Izv. Akad. Nauk Belorussk. SSR* (5) 81 (1987)
40. Brorson S D et al. *Phys. Rev. Lett.* **64** 2172 (1990)
41. Martynenko Yu V, Yavlinskii Yu N *Poverkhnost': Fiz., Khim., Mekh.* (6) 5 (1988)
42. Toulemonde M, Paumier E, Dufour Ch *Radiat. Eff. Defects Solids* **126** 201 (1993)
43. Komarov F F *Ionnaya Implantatsiya v Metally* (Ion Beam Modification of Metals) (Moscow: Metallurgiya, 1990) [Translated into English (Philadelphia: Gordon & Breach, 1992)]
44. Ziemann P, Miehle W, Plewnia A *Nucl. Instrum. Meth. B* **80/81** 370 (1993)
45. Paumier E et al. *Radiat. Eff. Defects Solids* **126** 181 (1993)
46. Bitensky I S, Parilis E S *Nucl. Instrum. Meth. B* **21** 26 (1987)
47. Kalinichenko A I, Lazurik-El'tsufin V T *Zh. Eksp. Teor. Fiz.* **65** 2364 (1973) [*Sov. Phys. JETP* **38** 1181 (1974)]
48. Borin I P et al. *Fiz. Tverd. Tela* **20** 2222 (1978)
49. Lagrand P, Morillo J, Pontikis V *Radiat. Eff. Defects Solids* **126** 51, 163 (1993)
50. Fleischer R L, Price P B, Walker R M *Nuclear Tracks in Solids* (Berkeley, Calif.: Univ. of California Press, 1975)
51. Klaumünzer S, Ming-dong Hou, Schumacher G *Phys. Rev. Lett.* **57** 850 (1986)
52. Ritchie R H, Claussen C *Nucl. Instrum. Meth. Phys. Res.* **198** 133 (1982)
53. Belyĭ V A, Komarov F F *Zh. Tekh. Fiz.* **68** (9) 42 (1998) [*Tech. Phys.* **43** 1048 (1998)]
54. Watson C C, Tombrello T A *Radiat. Eff.* **89** 263 (1983)
55. Komarov F F, Komarov A F *Vakuumnaya Tekh. Tekhnol.* **4** (1) 3 (1994)
56. Bringa E M, Johnson R E *Nucl. Instrum. Meth. B* **143** 513 (1998)
57. Bringa E M, Johnson R E, Dutkiewicz L *Nucl. Instrum. Meth. B* **152** 267 (1999)
58. Barbu A et al. *MRS Bull.* **20** (12) 29 (1995)
59. Dunlop A, Lesueur D, Barbu A *J. Nucl. Mater.* **205** 426 (1993)
60. Barbu A et al. *Mater. Sci. Forum* **97 – 99** 577 (1992)
61. Baranov I A et al. *Usp. Fiz. Nauk* **156** 477 (1988) [*Sov. Phys. Usp.* **31** 1015 (1988)]
62. Lapteva F S, Ershler B V *At. Energ.* **1** (4) 63 (1956)
63. Birtcher R C et al. *Phys. Rev. Lett.* **85** 4968 (2000)
64. Cheblukov Yu N et al., Scientific Report (Darmstadt, 1989)
65. Komarov F F *J. Langmuir* **12** 199 (1996)
66. Legg K O, Whaley R, Thomas E W *Surf. Sci.* **109** 11 (1981)
67. Vorob'eva I V, Geguzin L E, Monastyrenko V E *Fiz. Tverd. Tela* **28** 163 (1986) [*Sov. Phys. Solid State* **28** 88 (1986)]
68. Didyk A Yu et al. *Pis'ma Zh. Tekh. Fiz.* **26** (2) 1 (2000) [*Tech. Phys. Lett.* **26** 46 (2000)]
69. Didyk A Yu et al. *Perspektivnye Materialy* (1) 58 (2001)
70. Yavlinskiĭ Yu *Nucl. Instrum. Meth. B* **146** 142 (1998)
71. Hou V D, Klaumunzer S, Schumacher G *Nucl. Instrum. Meth. B* **19/20** 16 (1987)
72. Audouard A et al. *Radiat. Eff. Defects Solids* **126** 63 (1993)
73. Benyagoub A, Klaumunzer S *Radiat. Eff. Defects Solids* **126** 105 (1993)
74. Garrido F et al. *Radiat. Eff. Defects Solids* **126** 129 (1993)
75. Gutzmann A et al. *Radiat. Eff. Defects Solids* **126** 133 (1993)
76. Garrido F et al. *Phys. Rev. B* **52** 6273 (1995)
77. Audouard A et al. *Nucl. Instrum. Meth. B* **107** 185 (1996)
78. Benyagoub A et al. *Nucl. Instrum. Meth. B* **107** 189 (1996)
79. Rao B V et al. *Nucl. Instrum. Meth. B* **129** 487 (1997)
80. Komarov F F, Komarova V S *Vakuumnaya Tekh. Tekhnol.* **4** (4) 32 (1994)
81. Ryazanov A I, Volkov A E, Klaumünzer S *Phys. Rev. B* **51** 12107 (1995)
82. Trinkaus H *J. Nucl. Mater.* **223** 196 (1995)
83. Trinkaus H, Ryazanov A I *Phys. Rev. Lett.* **74** 5072 (1995)

84. Trinkaus H *Nucl. Instrum. Meth. B* **107** 155 (1996)
85. Trinkaus H *Nucl. Instrum. Meth. B* **146** 204 (1998)
86. Ryazanov A I, Trinkaus H, Volkov A E *Phys. Rev. Lett.* **84** 919 (2000)
87. Pacaud J et al. *Radiat. Eff. Defects Solids* **126** 369 (1993)
88. Leguay R, Dunlop A, Chevallier J *Radiat. Eff. Defects Solids* **126** 159 (1993)
89. Marfaing J et al. *Appl. Surf. Sci.* **46** 422 (1990)
90. Richomme F et al. *Nucl. Instrum. Meth. B* **107** 374 (1996)
91. Juraszek J et al. *Phys. Rev. B* **61** 12 (2000)
92. Nagel R, Balogh A G *Nucl. Instrum. Meth. B* **156** 135 (1999)
93. Senkara J et al. *Elektronica* (Poland) (11) 11 (1999)
94. Wang L et al. *Radiat. Eff. Defects Solids* **126** 403 (1993)
95. Matsumoto N et al. *Nucl. Instrum. Meth. B* **80/81** 428 (1993)
96. Adavi M A et al. *Izv. Ross. Akad. Nauk, Ser. Metally* (4) 93 (1995)
97. Jain A et al. *Vacuum* **46** 369 (1995)
98. Didyk A Yu *Izv. Ross. Akad. Nauk, Ser. Metally* (3) 128 (1995)
99. Toulemonde M et al. *Phys. Status Solidi A* **114** 467 (1989)
100. Mary P et al. *Nucl. Instrum. Meth. B* **62** 391 (1992)
101. Levalois M, Bogdanski P, Toulemonde M *Nucl. Instrum. Meth. B* **63** 14 (1992)
102. Marie P, Levalois M, Paumier E *J. Appl. Phys.* **79** 7555 (1996)
103. Mikou M et al. *Nucl. Instrum. Meth. B* **107** 246 (1996)
104. Bhatia K L et al. *Nucl. Instrum. Meth. B* **94** 379 (1994)
105. Varichenko V S et al., Preprint No. P14-95-74 (Dubna: JINR, 1995)
106. Varichenko V S et al. *Nucl. Instrum. Meth. B* **107** 268 (1996)
107. Zhu Zh et al. *Nucl. Instrum. Meth. B* **135** 260 (1998)
108. Levalois M, Marie P *Nucl. Instrum. Meth. B* **156** 64 (1999)
109. Vlasukova L A, Komarov A A, Komarov F F, in *Trudy IX Mezhnats. Soveshch. "Radiatsionnaya Fizika Tverdogo Tela"* (Proc. 9th Interethnic Conf. on Radiation Physics of Solids) Vol. 1 (Sevastopol', Ukraine, 1999) p. 252
110. Mikou M et al. *J. Phys. III* (Paris) **7** 1661 (1997)
111. Dunlop A, Jaskierowicz G, Della-Negra S *Nucl. Instrum. Meth. B* **146** 302 (1998)
112. Canut B et al. *Nucl. Instrum. Meth. B* **146** 296 (1998)
113. Izui K *J. Phys. Soc. Jpn.* **20** 915 (1965)
114. Furuno S et al. *Nucl. Instrum. Meth. B* **107** 223 (1996)
115. Antonova I A et al. *Phys. Status Solidi A* **147** K1 (1995)
116. Bourret A, Angert N, Grandin J P (Eds) *Proc. of the 3rd Intern. Symp. on Swift Heavy Ions in Matter, Caen, France, 15–19 May, 1995* (Nucl. Instrum. Meth. B, Vol. 107) (Amsterdam: North-Holland, 1996); see also references cited therein
117. Karamyan S A *Nucl. Instrum. Meth. B* **51** 354 (1990)
118. Wesch W et al. *Nucl. Instrum. Meth. B* **96** 290 (1995)
119. Chavan S T et al. *J. Appl. Phys.* **78** 2328 (1995)
120. Lhermitte-Sebire et al. *Philos. Mag. A* **69** 237 (1994)
121. Lhermitte-Sebire et al. *J. Mater. Sci.* **30** 2115 (1995)
122. Zaitsev A M *Mater. Sci. Eng. B* **11** 179 (1992)
123. Zaitsev A M et al. *Nucl. Instrum. Meth. B* **82** 421 (1993)
124. Varichenko V S et al., Preprint No. P14-95-181 (Dubna: JINR, 1995)
125. Varichenko V S et al., Preprint No. P14-95-145 (Dubna: JINR, 1995)
126. Ertchak D P, Efimov V G, Stelmakh V F *J. Appl. Spectrosc.* **64** 433 (1997)
127. Vetter J, Scholz R, Angert N *Nucl. Instrum. Meth. B* **91** 129 (1994)
128. Bursil L A, Braunshausen G *Philos. Mag. A* **62** 395 (1994)
129. Zaitsev A M *Radiat. Eff. Defects Solids* **126** 247 (1993)
130. Hedbabny H-J, Rogalla H *J. Appl. Phys.* **63** 2086 (1988)
131. Guimares R B et al. *J. Mater. Res.* **3** 1422 (1988)
132. Chadderton L T et al. *Nucl. Instrum. Meth. B* **91** 71 (1994)
133. Bitensky I S, Demirev P, Sundqvist B U R *Nucl. Instrum. Meth. B* **82** 356 (1993)
134. Beloshitsky V V, Komarov F F, Kumakhov M A *Phys. Rep.* **B 9** (3) 294 (1996)
135. Didyk A Yu, Varichenko V S, Zaĭtsev A M, Preprint No. P14-95-144 (Dubna: JINR, 1995)
136. Vorob'eva I V, Monastyrenko V E, Perelygin V P *Fiz. Tverd. Tela* **31** (10) 1 (1989) [*Sov. Phys. Solid State* **31** 1653 (1989)]
137. Burenkov A F, Komarov F F, Fedotov S A *Phys. Status Solidi B* **169** 33 (1992)
138. Burenkov A F, Komarov F F, Fedotov S A *Nucl. Instrum. Meth. B* **67** 30 (1992)
139. Burenkov A F, Komarov F F, Fedotov S A *Nucl. Instrum. Meth. B* **67** 35 (1992)
140. Burenkov A F et al. *Radiat. Eff. Defects Solids* **125** 169 (1993)
141. Komarov F F, Komarov A F *Zh. Eksp. Teor. Fiz.* **113** 489 (1998) [*JETP* **86** 270 (1998)]
142. Kumakhov M A, Shirmer G *Atomic Collisions in Crystals* (New York: Gordon and Breach Sci. Publ., 1989) Ch. 3
143. Burenkov A F et al. *Phys. Status Solidi A* **115** 427 (1989)
144. Biró L P et al., in *Proc. of the Mater. Res. Soc. Spring Meeting, Carbon Symp.* (Strasbourg, 1998) p. 1
145. Herre O et al. *Phys. Rev. B* **58** 4832 (1998)
146. Gaiduk P I et al. *Nukleonika* **44** 189 (1999)
147. Gaiduk P I et al., in *Proc. of the 1st Intern. Symp. "Ion Implantation and Other Application of Ions and Electrons"* (Poland: Nalenchov, 1997) p. 48
148. Wesch W et al. *Nucl. Instrum. Meth. B* **146** 341 (1998)
149. Gaiduk P I, Komarov F F, Wesch W *Nucl. Instrum. Meth. B* **164/165** 377 (2000)
150. Gaiduk P I et al. *Phys. Rev. B* **61** 15785 (2000)
151. Komarov F F, Komarov A A *Vakuumnaya Tekh. Tekhnol.* **8** (1) 3 (1998)
152. Komarov F F et al. *Vacuum* **70** 75 (2003)
153. Chew N G, Cullis A G *Ultramicrose* **23** 175 (1987)
154. Childs G E, Eriks L J, Powell R L *Thermal Conductivity of Solids at Room Temperature and Below* (NBS Monograph, 131) (Washington: NBS, 1973)
155. Amelinckx S, van Landuyt J, in *Diffraction and Imaging Techniques in Materials Science* Vol. 1 2nd ed. (Eds S Amelinckx, R Gevers, J van Landuyt) (Amsterdam: North-Holland, 1978) p. 107
156. Vohra Y K et al. *Phys. Rev. Lett.* **56** 1944 (1986)
157. Dartyge E, Sigmund P *Phys. Rev. B* **32** 5429 (1985)
158. Studer F et al. *Nucl. Instrum. Meth. B* **122** 449 (1997)
159. Tombrello T A et al. *Phys. Lett. A* **100** 42 (1984)
160. Belyi V A, Komarov F F, in *Proc. II Intern. Conf. "Ion Implantation and Other Application of Ions and Electrons"* (Lublin: Poland, 1998) p. 171
161. Belyi V A, Komarov F F *Nucl. Instrum. Meth. B* (2003) (to be published)
162. Martynenko Yu V, Yavlinskiĭ Yu N *At. Energ.* **62** 80 (1987)
163. Volkov A E, Borodin V A *Nucl. Instrum. Meth. B* **107** 172 (1996)
164. Komarov F F, Belyĭ V A *Zh. Eksp. Teor. Fiz.* **122** 366 (2002) [*JETP* **95** 316 (2002)]
165. Bohr N "The penetration of atomic particles through matter" *Kgl. Danske Videnskab. Selskab. Mat.–Fys. Medd.* **18** (8) (1948) [Translated into Russian (Moscow: IL, 1950)]
166. Kumakhov M A, Komarov F F *Energy Loss and Ranges of Ions in Solids* (New York: Gordon and Breach, 1989)
167. Betz H-D *Rev. Mod. Phys.* **44** 465 (1972)
168. Martin F W *Phys. Rev. Lett.* **22** 329 (1969)
169. Moak C D *Phys. Rev. B* **10** 2681 (1974)
170. Datz Sh *Radiat. Eff.* **12** 163 (1972)
171. Dmitriev I S, Nikolaev V S *Zh. Eksp. Teor. Fiz.* **47** 615 (1964) [*Sov. Phys. JETP* **20** 409 (1965)]
172. Ziegler J F, Biersack J P, Littmark U *The Stopping and Range of Ions in Solids* (New York: Pergamon Press, 1985)
173. Chadderton L T, Torrens I M *Fission Damage in Crystals* (London: Methuen, 1969)
174. Matzke H J *Radiat. Eff.* **64** 3 (1982)
175. Fischer B E, Spohr R *Rev. Mod. Phys.* **55** 907 (1983)
176. Balanzat E, Jousset J C, Toulemonde M *Nucl. Instrum. Meth. B* **32** 368 (1988)
177. Toulemonde M et al. *Nucl. Instrum. Meth. B* **39** 1 (1989)
178. Studer F et al. *Radiat. Eff. Defects Solids* **110** 55 (1990)
179. Studer F, Toulemonde M *Nucl. Instrum. Meth. B* **65** 560 (1992)
180. Komarov F F, Komarova V S *Vacuum Tech. Technol.* **4** (2) 21 (1994)
181. Provost J et al. *MRS Bull.* **20** (12) 22 (1995)
182. Toulemonde M *Nucl. Instrum. Meth. B* **156** 1 (1999)
183. Toulemonde M et al. *Nucl. Instrum. Meth. B* **166/167** 903 (2000)
184. Silk E C M, Barnes R S *Philos. Mag.* **7** 970 (1959)
185. Price P B, Walker R M *Phys. Rev. Lett.* **8** 217 (1962)
186. Trautmann C et al. *Mater. Res. Symp. Proc.* **504** 123 (1989)

187. Schwartz K et al. *Phys. Rev. B* **58** 11232 (1998)
188. Meftah A et al. *Phys. Rev. B* **48** 920 (1993)
189. Itoh N, Stoneham A M *Nucl. Instrum. Meth. B* **146** 362 (1998)
190. Trautmann C et al. *Nucl. Instrum. Meth. B* **164/165** 365 (2000)
191. Canut B et al. *Phys. Rev. B* **51** 12194 (1995)
192. Canut B et al. *Nucl. Instrum. Meth. B* **107** 194 (1996)
193. Fleischer R L *MRS Bull.* **20** (12) 17 (1995)
194. Tombrello T A *Nucl. Instrum. Meth. B* **83** 508 (1993)
195. Tombrello T A *Nucl. Instrum. Meth. B* **94** 424 (1994)
196. Tombrello T A *Nucl. Instrum. Meth. B* **95** 232 (1995)
197. Tombrello T A, Childs A M, Hartman J W *Nucl. Instrum. Meth. B* **145** 429 (1998)
198. Chadderton L T, Montagu-Pollok H *Proc. R. Soc. London Ser. A* **274** 239 (1969)
199. Bonfiglioli G, Ferro A, Mojoni A *J. Appl. Phys.* **32** 2499 (1961)
200. Watson C C, Tombrello T A *Radiat. Eff.* **89** 263 (1985)
201. Meftah A et al. *Phys. Rev. B* **49** 12457 (1994)
202. Meftah A et al. *Nucl. Instrum. Meth. B* **122** 470 (1997)
203. Naguib H M, Kelly R *Radiat. Eff.* **25** 1 (1975)
204. Katin V V, Martynenko Yu V, Yavlinskiĭ Yu N *Pis'ma Zh. Tekh. Fiz.* **13** 665 (1987) [*Sov. Tech. Phys. Lett.* **13** 276 (1987)]
205. Szenes G *Phys. Rev. B* **52** 6154; **51** 8026 (1995)
206. Szenes G *Nucl. Instrum. Meth. B* **116** 141 (1996)
207. Szenes G *Nucl. Instrum. Meth. B* **122** 530 (1997)
208. Yavlinskii Yu N *Nucl. Instrum. Meth. B* **166/167** 35 (2000)
209. Itoh N *Nucl. Instrum. Meth. B* **122** 405 (1997)
210. Yavlinskii Yu *Nucl. Instrum. Meth. B* **146** 142 (1998)
211. Agullo-Lopez F, Lopez F J, Jacue F *Cryst. Latt. Def. Amorph. Mat.* **9** 227 (1987)
212. Lushchik Ch B, in *Physics of Radiation Effects in Crystals* (Modern Problems in Condensed Matter Sciences, Vol. 13, Eds R A Johnson, A N Orlov) (Amsterdam: North-Holland, 1986) p. 473
213. Itoh N, Tanimura K *J. Phys. Chem. Solids* **5** 717 (1980)
214. Popov A I, Balanzat E *Nucl. Instrum. Meth. B* **166/167** 545 (2000)
215. Müller A et al. *Appl. Phys. A* **66** 1147 (1989)
216. Müller A et al. *Nucl. Instrum. Meth. B* **146** 393 (1998)
217. Trautmann C, Schwartz K, Steckenreiter T *Nucl. Instrum. Meth. B* **156** 162 (1999)
218. Schwartz K et al. *Phys. Rev. B* **56** 10711 (1997)
219. Jensen J, Dunlop A, Della-Negra S *Nucl. Instrum. Meth. B* **141** 753 (1998)
220. Pariselle M A et al. *Nucl. Instrum. Meth. B* **166/167** 538 (2000)
221. Houpert Ch et al. *Nucl. Instrum. Meth. B* **39** 720 (1989)
222. Costantini J M et al. *Nucl. Instrum. Meth. B* **65** 568 (1992)
223. Costantini J M et al. *J. Appl. Phys.* **87** 1899 (2000)
224. Meftah A et al. *Phys. Rev. B* **48** 920 (1993)
225. Costantini J M et al. *Nucl. Instrum. Meth. B* **91** 288 (1994)
226. Szenes G et al. *Nucl. Instrum. Meth. B* **166/167** 949 (2000)
227. Dartyge E et al. *Phys. Rev. B* **23** 5213 (1981)
228. Albrecht D et al. *Appl. Phys. A* **37** 37 (1985)
229. Biró L P, Gyulai J, Havanesák K *Nucl. Instrum. Meth. B* **122** 476 (1997)
230. Chailley V, Dooryhée E, Levalois M *Nucl. Instrum. Meth. B* **107** 199 (1996)
231. Vetter J et al. *Nucl. Instrum. Meth. B* **141** 747 (1998)
232. Vorobyova I V, Reimann C T, Toulemonde M *Nucl. Instrum. Meth. B* **166/167** 959 (2000)
233. Neumann R *Nucl. Instrum. Meth. B* **151** 42 (1999)
234. Simon Ch et al. *Nucl. Instrum. Meth. B* **107** 384 (1996)
235. Hardy V et al. *Radiat. Eff. Defects Solids* **118** 343 (1991)
236. Hardy V et al. *Physica C* **191** 85 (1992)
237. Hirata K *Nucl. Instrum. Meth. B* **156** 12 (1999)
238. Indenbom M V et al. *Phys. Rev. Lett.* **84** 1792 (2000)
239. Toulemonde M et al. *Nucl. Instrum. Meth. B* **116** 37 (1996)
240. Douillard L, Duraud J P *Nucl. Instrum. Meth. B* **107** 212 (1996)
241. Canut B et al. *Nucl. Instrum. Meth. B* **91** 312 (1994)
242. Ramos S M M et al. *Nucl. Instrum. Meth. B* **107** 254 (1996)
243. Opfermann Th et al. *Nucl. Instrum. Meth. B* **166/167** 954 (2000)
244. Wiss T et al. *Nucl. Instrum. Meth. B* **122** 583 (1997)
245. Matzke Hj, Lucuta P G, Wiss T *Nucl. Instrum. Meth. B* **166/167** 920 (2000)
246. Ghidini M et al. *Nucl. Instrum. Meth. B* **107** 344 (1996)
247. Hemon S et al. *Nucl. Instrum. Meth. B* **122** 526 (1997)
248. Berthelot A et al. *Nucl. Instrum. Meth. B* **166/167** 927 (2000)
249. Rodichev D et al. *Nucl. Instrum. Meth. B* **107** 259 (1996)
250. Marty J M et al. *Nucl. Instrum. Meth. B* **91** 274 (1994)
251. Thevenard P A et al. *MRS Symp. Proc.* **396** 127 (1996)
252. Skuratov V A, Abu-Alazm S M, Altynov V A *Mater. Sci. Forum* **248** 399 (1997)
253. Aruga T et al. *Nucl. Instrum. Meth. B* **166/167** 913 (2000)
254. Hobbs L W et al. *Nucl. Instrum. Meth. B* **116** 18 (1996)
255. Zinkle S J, Pells G P *J. Nucl. Mater.* **253** 120 (1998)
256. Zinkle S J, Skuratov V A *Nucl. Instrum. Meth. B* **141** 737 (1998)
257. Ferain E, Legras R *Nucl. Instrum. Meth. B* **174** 116 (2001)
258. Fleischer R *MRS Bull.* **20** (12) 35 (1995)